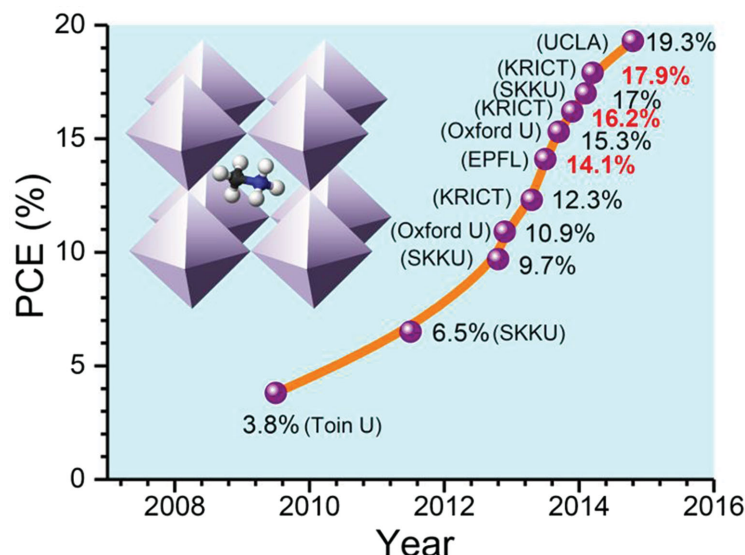


# Perovskite Solar Cells: From Materials to Devices

Hyun Suk Jung\* and Nam-Gyu Park\*



## From the Contents

1. Historical Background of Organometal Halide Perovskites..... 11
2. Basic Fundamentals of Organometal Halide Perovskites..... 11
3. Working Principle and Device Structures ... 13
4. Preparation Methods for High Efficiency Perovskite Solar Cells..... 15
5. Photoluminescence and Polarization Characteristics..... 18
6. Perovskite Suitable for Flexible Solar Cells ..... 21
7. Long-Term Stability ..... 22
8. Summary and Outlook..... 23

**Perovskite solar cells based on organometal halide light absorbers have been considered a promising photovoltaic technology due to their superb power conversion efficiency (PCE) along with very low material costs.** Since the first report on a long-term durable solid-state perovskite solar cell with a PCE of 9.7% in 2012, a PCE as high as 19.3% was demonstrated in 2014, and a certified PCE of 17.9% was shown in 2014. Such a high photovoltaic performance is attributed to optically high absorption characteristics and balanced charge transport properties with long diffusion lengths. Nevertheless, there are lots of puzzles to unravel the basis for such high photovoltaic performances. The working principle of perovskite solar cells has not been well established by far, which is the most important thing for understanding perovskite solar cells. In this review, basic fundamentals of perovskite materials including optoelectronic and dielectric properties are described to give a better understanding and insight into high-performing perovskite solar cells. In addition, various fabrication techniques and device structures are described toward the further improvement of perovskite solar cells.

# 1. Historical Background of Organometal Halide Perovskites

The key material for the perovskite solar cell recently receiving great attention is the organometal halide  $\text{CH}_3\text{NH}_3\text{MX}_3$  ( $\text{M} = \text{Pb}$  or  $\text{Sn}$ ,  $\text{X} = \text{Cl}$ ,  $\text{Br}$  or  $\text{I}$ ), whose structure and physical properties were first reported by Weber in 1978.<sup>[1,2]</sup> Those Pb- and Sn-based halide perovskite materials were stabilized mostly as cubic perovskite structures at ambient temperature. For  $\text{CH}_3\text{NH}_3\text{PbX}_3$ , the unit cell parameter  $a$  increases from 5.68 to 5.92 and to 6.27 Å as the size of halide increases from  $\text{X} = \text{Cl}$  to  $\text{Br}$  and to  $\text{I}$ , respectively. Lattice parameters in the cubic phase can be simply tuned by mixing halides; for instance,  $\text{CH}_3\text{NH}_3\text{PbBr}_{2.3}\text{Cl}_{0.7}$  showed  $a = 5.98$  Å,  $\text{CH}_3\text{NH}_3\text{PbBr}_{2.07}\text{I}_{0.93}$  showed  $a = 6.03$  Å, and  $\text{CH}_3\text{NH}_3\text{PbBr}_{0.45}\text{I}_{2.55}$  showed  $a = 6.25$  Å.  $\text{CH}_3\text{NH}_3\text{SnBr}_x\text{I}_{3-x}$  ( $x = 0$ –3) crystallized to the cubic perovskite structure with the unit cell parameters  $a = 5.89$  Å ( $x = 3$ ),  $a = 6.01$  Å ( $x = 2$ ) and  $a = 6.24$  Å ( $x = 0$ ). Contrary to Pb-based perovskite materials, some Sn-based perovskite materials exhibited conducting properties.<sup>[2]</sup>

Organic–inorganic perovskites have received attention due to their being capable of undergoing a transition from insulator to metal by increasing the number of inorganic layers in the  $(\text{C}_4\text{H}_9\text{NH}_3)_2(\text{CH}_3\text{NH}_3)_{n-1}\text{Sn}_n\text{I}_{3n+1}$  layered perovskite.<sup>[3]</sup> This result was considered to be an important finding because high-temperature superconductors could be possible from these organic–inorganic perovskite materials. For this reason, little attention has been paid to the photovoltaic ability of the organic–inorganic halide perovskite materials. In 2009, it was first attempted to use  $\text{CH}_3\text{NH}_3\text{PbX}_3$  ( $\text{X} = \text{Br}$  and  $\text{I}$ ) as a semiconductor sensitizer in dye-sensitized liquid junction-type solar cells.<sup>[4]</sup> This attempt led to the power conversion efficiency (PCE) of 3–4%, which was, however, a much low efficiency compared to the conventional Ru-based molecular dyes with PCEs of more than 11%<sup>[5]</sup> and even semiconductor quantum dot sensitizers with PCEs of 5–6%.<sup>[6]</sup> Thus, little attention has been focused on the methylammonium lead halide perovskite materials due to their low photovoltaic performance and extreme instability to liquid electrolytes. Park's group reported two years later a 6.5% efficient  $\text{CH}_3\text{NH}_3\text{PbI}_3$  perovskite solar cell which was slightly more stable in electrolytes.<sup>[7]</sup> This result contained more advanced technology, showing how to form the perovskite sensitizer on the thinner  $\text{TiO}_2$  film. However, this result was not cited until the development of a long-term stable perovskite solar cell in 2012<sup>[8]</sup> due to the dissolution problem of the organic–inorganic halide perovskite in polar liquid electrolytes. Perovskite solar cell research has been triggered by the discovery of the 9.7% solid-state perovskite solar cell with a 500 h confirmed stability.<sup>[8]</sup>

## 2. Basic Fundamentals of Organometal Halide Perovskites

### 2.1. Madelung Constant and Lattice Energy

The Madelung constant ( $M$ ) for cubic perovskite  $\text{A}^{+1}\text{B}^{+2}(\text{X}^{-1})_3$  was estimated to be related to the Madelung

constant for the CsCl structure and the  $\text{Cu}_2\text{O}$  structure, that is,  $M(\text{A}^{+1}\text{B}^{+2}(\text{X}^{-1})_3) = 2M(\text{Cu}_2\text{O}) - 4M(\text{CsCl})$ .<sup>[9]</sup> The Madelung constant is important in evaluating lattice energy. Based on the knowledge that Madelung constants for  $\text{Cu}_2\text{O}$  and CsCl are 4.4425 and 1.7627, respectively,<sup>[10]</sup> the Madelung constant for organometal halide perovskites with cubic structures are calculated to be 1.8342. Since the lattice energy is proportional to the Madelung constant and oxidation numbers (i.e., ionic charges) according to the Born–Landé equation,<sup>[11]</sup> the lattice energy can be roughly estimated from those values. For instance, the ratio of lattice energies ( $E_{\text{lat}}$ ) between  $\text{Cu}_2\text{O}$  and CsCl will be  $E_{\text{lat}}(\text{Cu}_2\text{O})/E_{\text{lat}}(\text{CsCl}) = 5.0406$ , because  $E_{\text{lat}}(\text{Cu}_2\text{O}) \propto 4.4425 \times (+1) \times (-2)$  and  $E_{\text{lat}}(\text{CsCl}) \propto 1.7627 \times (+1) \times (-1)$ , which is consistent with the ratio of 4.9817 calculated from the lattice energies for  $\text{Cu}_2\text{O}$  (3273 kJ/mol) and CsCl (657 kJ/mol), estimated based on the standard thermochemical properties of chemical substances.<sup>[12]</sup> Thus the lattice energy of  $\text{ABX}_3$  cubic perovskite is expected to be higher than that of CsCl but lower than that of  $\text{Cu}_2\text{O}$ , because  $E_{\text{lat}}(\text{ABX}_3) \propto 1.8342 \times (+1) \times (+2) \times (-1)$ , from which one can expect that only a low energy is required to separate the perovskite solid into ions and to form the perovskite from ions because of ionic characteristics. In addition, the covalency of the ionic crystal will increase as the lattice energy increases, or ionicity increases as lattice energy decreases.<sup>[13]</sup> For instance, the enhanced bond ionicity was found to decrease the lattice energy and thereby improve the dielectric properties.<sup>[13]</sup> Thus, organometal halide perovskite tends to possess strong ionic characteristics due to its low lattice energy, which is likely to be sensitive to polarization in an electric field.

### 2.2. Phase Transition and Its Origin

It is interesting that methylammonium ( $\text{MA} = \text{CH}_3\text{NH}_3^+$ )-based halide perovskite materials undergo structural phase transitions with temperature, due to the molecular motion of the methylammonium cation along the C–N axis and/or with respect to the crystal axis, as can be seen in Figure 1.<sup>[14]</sup> The degree of rotation of  $\text{CH}_3\text{NH}_3^+$  was investigated using  $^1\text{H}$  and  $^{14}\text{N}$  NMR spectra, where a rapid rotation was observed at high temperature phases and its rotation was restricted when

H. S. Jung  
School of Advanced Materials  
Science and Engineering  
Sungkyunkwan University (SKKU)  
Suwon 440–746, Korea  
Tel: 82–31–290–7403  
E-mail: hsjung1@skku.edu

N.-G. Park  
School of Chemical Engineering and  
Department of Energy Science  
Sungkyunkwan University (SKKU)  
Suwon 440–746, Korea  
Tel: 82–31–290–7241  
E-mail: npark@skku.edu



DOI: 10.1002/smll.201402767

the temperature was lowered.<sup>[14]</sup> The temperature-dependent crystal structure of MAPbX<sub>3</sub> was studied with the powdered samples, where cubic → tetragonal → orthorhombic phase transitions were detected as the temperature was lowered due to highly ordered organic cations along the C–N axis, via the quenching of molecular motion.<sup>[15]</sup>

Recent first principle calculations for CH<sub>3</sub>NH<sub>3</sub>PbI<sub>3</sub> revealed that the C–N bonds of MA ions are arranged in parallel along the *ab* plane that is perpendicular to the *c*-axis, i.e., the (002) or (004) planes in the low-temperature orthorhombic phase, whereas they are distributed vertically and in parallel in the room-temperature tetragonal phase.<sup>[17]</sup> The distribution of MA ions does not directly affect the valence band maximum (VBM) and conduction band minimum (CBM), but has an influence on Pb–I bond length, Pb–I–Pb bond angle, and bandgap energy, which indicates that the MA ions play an important role in both the geometry stability and the electronic structure.<sup>[17]</sup>

### 2.3. Band Position and Bandgap Tuning

The absorption coefficient of CH<sub>3</sub>NH<sub>3</sub>PbI<sub>3</sub> was estimated to be  $1.5 \times 10^4 \text{ cm}^{-1}$  at 550 nm from a nanocrystalline TiO<sub>2</sub> thin film whose surface was coated with CH<sub>3</sub>NH<sub>3</sub>PbI<sub>3</sub> nanodots,<sup>[7]</sup> which indicates that the penetration depth for 550 nm light is only 0.66 μm. The absorption property of a thin CH<sub>3</sub>NH<sub>3</sub>PbI<sub>3</sub> perovskite film was measured and compared to those of conventional photovoltaic materials such as GaAs, CdTe, and CIGS, where the absorption coefficients are as high as  $10^4$ – $10^5 \text{ cm}^{-1}$  and the sharp onset near the bandgap for perovskite was similar to those for the typical photovoltaic materials.<sup>[18]</sup> The bandgap of CH<sub>3</sub>NH<sub>3</sub>PbI<sub>3</sub> was evaluated to be 1.50–1.55 eV from UV photoelectron, UV-vis, and incident photon-to-electron efficiency (IPCE) spectra.<sup>[8]</sup> However, a bandgap of around 1.55 eV is not enough for panchromatic absorption due to the relatively short absorption wavelength limited to 800 nm. Bandgap tuning is required to extend the absorption to longer wavelengths without sacrificing the absorption coefficient. Replacing MA with other organic cations is one approach, since organic cations in the A site of ABX<sub>3</sub> can tune the bandgap because they modify the M–X–M bond length and angle without affecting the valence band maximum.<sup>[17]</sup> For instance, the replacement of MA with formamidinium HC(NH<sub>2</sub>)<sub>2</sub><sup>+</sup> (FA) was found to reduce the bandgap by about 0.07 eV, giving rise to an extension of the absorption wavelength by about 40 nm.<sup>[19]</sup> Another approach is the direct modification of M–X bond. For instance, the bandgap decreases from 1.55 eV to 1.17 eV when partially replacing the Pb(2+) in CH<sub>3</sub>NH<sub>3</sub>PbI<sub>3</sub> with Sn(2+).<sup>[20]</sup> Thus, the bandgap can be tuned in between 1.55 eV and 1.17 eV by varying the ratio of lead to tin. Moreover, the direct modification of M–X bonds in AMX<sub>3</sub> perovskite will influence the valence band maximum (VBM) and conduction band minimum (CBM), since band edges are determined by the B-site metal orbitals as studied by the first principle calculations.<sup>[21]</sup> In CH<sub>3</sub>NH<sub>3</sub>PbI<sub>3</sub>, it was estimated that the VBM consisted mainly of the s-antibonding states of Pb 6s



He presently researches perovskite solar cells and flexible solar cells.

**Hyun Suk Jung** is an associate professor in the School of Advanced Materials Science & Engineering at Sungkyunkwan University (SKKU). He received his BS, MS, and PhD degrees in materials science and engineering from Seoul National University (SNU), in 1997, 1999, and 2004, respectively. He joined Los Alamos National Laboratory (LANL) as a director's postdoctoral fellow in 2005. He had worked for Kookmin University (KMU) since 2006 and joined SKKU in 2011. He has published over 110 peer-reviewed papers regarding the synthesis of inorganic nanomaterials and dye-sensitized solar cells.



Sungkyunkwan University (SKKU) as a full professor. He is currently a distinguished professor at SKKU. His research has been focused on dye-sensitized solar cells since 1997, and he is currently devoted to perovskite solar cells since the first report on a solid state perovskite solar cell in 2012 by his group.

**Nam-Gyu Park** received his BS in chemical education and MS and PhD degrees in chemistry from Seoul National University (SNU) in 1988, 1992, and 1995, respectively. He was at ICMCB-CNRS, France, from 1996 to 1997 and National Renewable Energy Laboratory (NREL), USA, from 1997 to 1999 as a postdoctoral researcher. He worked for the Electronics and Telecommunications Research Institute from 2000 to 2005. He was the director of the solar cell research center at Korea Institute of Science and Technology (KIST) from 2005 to 2009. Since 2009, he joined School of Chemical Engineering of

and I 5p orbitals, and the CBM was composed primarily of the s-antibonding states of Pb 6p and I 5s orbitals.<sup>[21]</sup> It is also obvious that changing the halide in the M–X bond will result in modification of the bandgap. Electronic structures of CH<sub>3</sub>NH<sub>3</sub>PbX<sub>3</sub> (X = Cl, Br, and I) and CH<sub>3</sub>NH<sub>3</sub>PbI<sub>2</sub>X were recently studied based on density functional theory (DFT) calculations,<sup>[22]</sup> where the calculated bandgaps were in agreement to some extent with the experimentally observed bandgaps for CH<sub>3</sub>NH<sub>3</sub>PbX<sub>3</sub> with tetragonal (1.66 (1.55), 1.83 (1.78), and 1.64 (1.55) eV for X = I, Br, and Cl, respectively. Parentheses are experimental values.) and cubic (1.57 (1.55), 1.80 (2.00), and 2.34 (3.11) eV for X = I, Br, and Cl, respectively) structures. **Figure 2** shows the bandgap, VBM, and CBM for ABX<sub>3</sub> (A = MA and FA, B = Pb, Sn or Sn<sub>1-x</sub>Pb<sub>x</sub>, X = Cl, Br, I or I<sub>1-x</sub>Br<sub>x</sub>).

Regarding the optical properties of some perovskite materials, Pb-based perovskite materials such as CH<sub>3</sub>NH<sub>3</sub>PbI<sub>3</sub> and HC(NH<sub>2</sub>)<sub>2</sub>PbI<sub>3</sub> exhibit higher absorption coefficients than Sn-based perovskite ones.<sup>[19]</sup> However, a contrary result was reported, where the computational calculation based on a GW method incorporating spin-orbit coupling (SOC) showed that the optical absorption of CH<sub>3</sub>NH<sub>3</sub>SnI<sub>3</sub> was higher than that of its Pb-based analogue.<sup>[23]</sup> Both the Pb- and Sn-based perovskite materials are promising candidates for high efficiency perovskite solar cells in terms of bandgap and absorption properties.



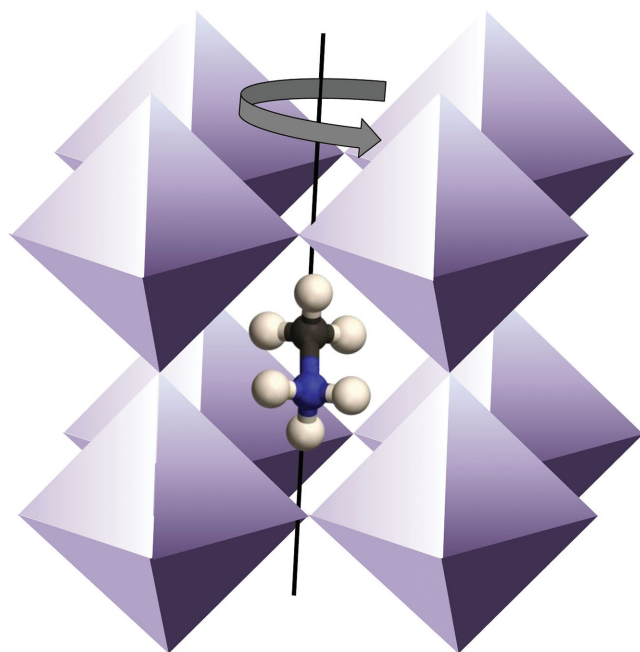


**Figure 1.** Molecular motion of A-site  $\text{CH}_3\text{NH}_3^+$  cation in the perovskite  $\text{CH}_3\text{NH}_3\text{MX}_3$  ( $M$  = divalent metal and  $X$  = halogen) unit cell.  $\text{CH}_3\text{NH}_3^+$  cation can have two types of orientational disorder in the crystal: the orientation of the C–N axis relative to the crystal axis (type A) and the rotation around the C–N axis (type B).<sup>[16]</sup>

## 2.4. Dielectric and Electrical Properties

Heat capacity, dielectric permittivity, AC and DC conductivity, and pressure–temperature phase relations of  $\text{MAPbX}_3$  ( $X = \text{Cl}, \text{Br}$  and  $\text{I}$ ) and  $\text{MASnX}_3$  ( $X = \text{Br}$  and  $\text{I}$ ) have been studied in detail.<sup>[16,24,25]</sup> The data were obtained from single crystals, where an aqueous solution of  $\text{Pb}(\text{CH}_3\text{CO}_2)_2$  was added dropwise to an excess quantity of hot aqueous solution of  $\text{MAX}$  ( $X = \text{Cl}, \text{Br}$ , and  $\text{I}$ ), followed by slow cooling to 5 °C for preparing  $\text{MAPbX}_3$  ( $X = \text{Cl}, \text{Br}$ , and  $\text{I}$ ) crystals. For preparing  $\text{MASnBr}_3$  crystals, an anhydrous ethanol solution

of  $\text{MABr}$  was added dropwise to a boiling ethanol solution of  $\text{SnBr}_2$ , which was slowly cooled in a dry  $\text{N}_2$  atmosphere. In this case,  $\text{SnBr}_2$  was recommended to be purified by sublimation in an evacuated glass tube. The  $\text{MASnI}_3$  crystal was grown at 170 °C for 3 days in a glass tube filled with He gas.

The real part of the dielectric permittivity (dielectric constant)  $\epsilon'$  was investigated with temperature (phase).  $\epsilon'$  was higher for the tetragonal phase in temperatures ranging from 180 to 300 K, compared to the orthorhombic phase at lower temperature, in which  $\epsilon'$  increased as the halide anion in  $\text{MAPbX}_3$  changed from  $\text{Cl}$  ( $\epsilon' \approx 40$  at 300 K and  $\approx 60$  at 200 K), to  $\text{Br}$  ( $\epsilon' \approx 50$  at 300 K and  $\approx 70$  at 200 K) and  $\text{I}$  ( $\epsilon' \approx 60$  at 300 K and  $\approx 100$  at 200 K) at 100 kHz. In the low-temperature orthorhombic phase,  $\epsilon'$  was as low as 17, 26, and 36 for  $\text{Cl}$ ,  $\text{Br}$  and  $\text{I}$ , respectively, and temperature independent, which indicates that electronic or ionic polarization is expected from the orthorhombic phase. **Figure 3** shows the dielectric constants as a function of frequency,<sup>[12]</sup> where electronic polarization arises when the local electronic charges around the nucleus are displaced under the electric field, and ionic polarization results from the displacement of cations and anions in opposite directions under an electric field in ionic materials, whereas orientational polarization can occur in substances with molecules that have permanent electric dipoles. The orientational polarizability ( $\alpha_{\text{or}}$ ) depends on temperature:  $\alpha_{\text{or}} = P^2/3kT$  where  $k$  is the Boltzmann constant and  $T$  temperature. Giant dielectric constants, approaching  $10^7$ , are observed from perovskites upon illumination especially at low frequencies, as shown in Figure 3b,<sup>[26]</sup> which is related to the molecular orientation of A-site  $\text{CH}_3\text{NH}_3^+$  ions.

$\text{Sn}$ -based perovskites such as  $\text{CsSnBr}_3$  and  $\text{CH}_3\text{NH}_3\text{SnI}_3$  were found to exhibit high electrical conductivity, which might be closely related to the infinite linear  $-\text{I}-\text{Sn}-\text{I}-\text{Sn}-$  chains formed three-dimensionally in the perovskite lattice.<sup>[28]</sup> For the case of  $\text{Sn}$ -based bromide perovskite materials, the  $\text{Sn}$  environment coordinated with bromide was found to be critical to determine the electrical properties. According to  $^{119}\text{Sn}$  Mössbauer studies on a series of solid solutions,  $\text{CH}_3\text{NH}_3\text{Sn}_{1-x}\text{Pb}_x\text{Br}_3$ , and  $\text{CsSnBr}_3$ , the high electrical conductivity of the  $\text{CsSnBr}_3$  (almost metallic) decreased drastically upon replacement of  $\text{Cs}$  and  $\text{Sn}$  by  $\text{CH}_3\text{NH}_3$  and  $\text{Pb}$ , respectively, due to change in the local octahedral environment of  $\text{SnBr}_6$  and the  $\text{Sn}-\text{Br}-\text{Sn}$  bond length.<sup>[29]</sup>

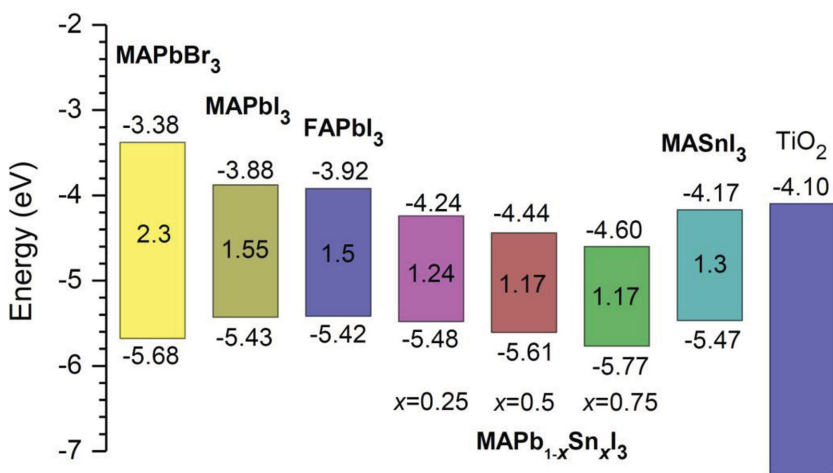


**Figure 2.** Schematic energy level diagram of  $\text{MAPbBr}_3$ ,  $\text{MAPbI}_3$ ,  $\text{FAPbI}_3$ ,  $\text{MAPb}_{1-x}\text{Sn}_x\text{I}_3$ , and  $\text{MASnI}_3$  along with  $\text{TiO}_2$ . MA and FA stand for methylammonium ( $\text{CH}_3\text{NH}_3$ ) and formamidinium ( $\text{HC}(\text{NH}_2)_2$ ), respectively. Data for  $\text{MAPb}_{1-x}\text{Sn}_x\text{I}_3$  ( $x = 0.25, 0.5, 0.75$  and 1) are reproduced with permission.<sup>[20]</sup> Copyright 2014, ACS.

## 3. Working Principle and Device Structures

Light absorption, charge separation, charge transport, and charge collection are general solar cell working processes. In order to construct them, light harvesters should be selected and their opto-electronic properties investigated. For instance, a p-i-n junction is required in case the light harvester is an intrinsic

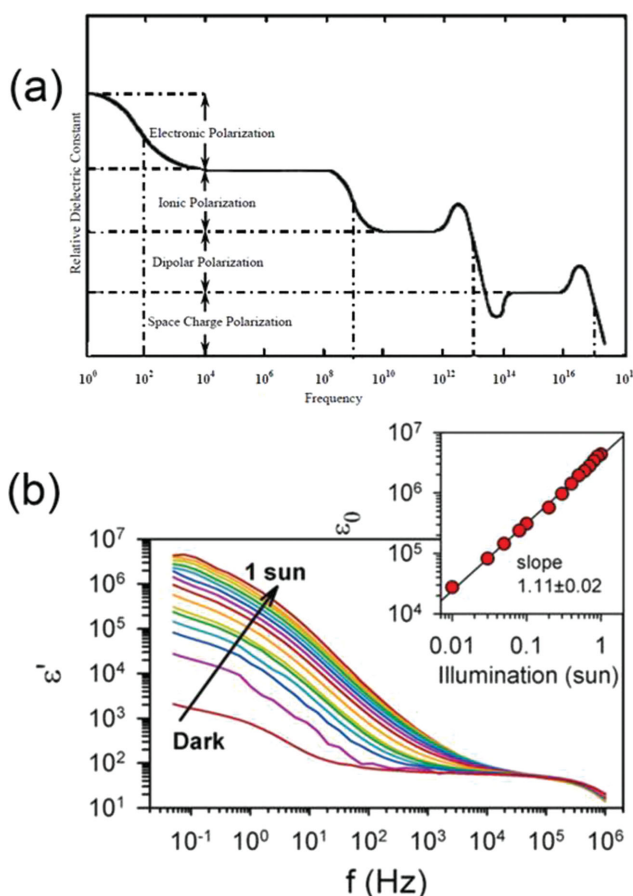


**Figure 3.** (a) Schematic of different contributions to polarizability as a function of frequency and (b) the real permittivity as a function of frequency for different incident light intensities from dark to 1 sun ( $100 \text{ mW/cm}^2$ ) for  $\text{MAPbI}_{3-x}\text{Cl}_x$  perovskite (compact  $\text{TiO}_2/\text{MAPbI}_{3-x}\text{Cl}_x$  in  $\text{Al}_2\text{O}_3$  scaffold/spiro-OMeTAD), measured at room temperature and 0 V applied bias. Reproduced with permission.<sup>[27]</sup> Inset: linear regression of dielectric constant vs. illumination intensity at  $f = 50 \text{ mHz}$ , observing a close-to-linear dependence between  $\epsilon_0$  and illumination intensity. Reproduced with permission.<sup>[26]</sup> Copyright 2014, ACS.

semiconductor, while a **p-n junction** is needed if the light harvester possesses **an n-type or p-type property, because n- or p-types can transfer electrons or holes to the light harvester**. Organometallic perovskite materials can be applied to either p-i-n junction or p-n junction types, since they have balanced charge transport properties. **Electron and hole transport properties were reported for**  $\text{CH}_3\text{NH}_3\text{PbI}_3$  prepared by different synthetic methods using a  $\text{CH}_3\text{NH}_3\text{I} + \text{PbI}_2$  mixture<sup>[30]</sup> and a  $3\text{CH}_3\text{NH}_3\text{I} + \text{PbCl}_2$  mixture,<sup>[31]</sup> where X-ray diffraction patterns were indexed as tetragonal  $\text{CH}_3\text{NH}_3\text{PbI}_3$  regardless of the preparation method. The electron and hole diffusion lengths were estimated to be  $\sim 130 \text{ nm}$  and  $\sim 100 \text{ nm}$ , respectively, for the samples prepared from the former method, while longer diffusion lengths of  $\sim 1069 \text{ nm}$  for electrons and  $\sim 1213 \text{ nm}$  for holes were measured for the sample prepared using the latter method. The difference in diffusion length depending on preparation method is likely to be due to quality of the perovskite layer, such as crystallinity or grain size. Electron beam-induced current (EBIC) imaging studies of  $\text{CH}_3\text{NH}_3\text{PbI}_3$  layers prepared from  $\text{PbI}_2$  and  $\text{PbCl}_2$  sources

revealed that charge diffusion lengths were about  $1 \mu\text{m}$  for both samples, but the diffusion length for holes was longer than that for electrons for the case of  $\text{CH}_3\text{NH}_3\text{PbI}_3$  prepared without a chloride source.<sup>[32]</sup> To compensate the shorter electron diffusion length, an electron transport layer with a long diffusion length may be required for  $\text{CH}_3\text{NH}_3\text{PbI}_3$ . Electron diffusion lengths of  $\text{CH}_3\text{NH}_3\text{PbI}_3$  solar cells employing mesoporous  $\text{TiO}_2$  layers are estimated to exceed  $1 \mu\text{m}$ .<sup>[33]</sup> Electron and hole mobilities were found to be as high as  $25 \text{ cm}^2/\text{Vs}$ , and the mobilities of both were almost balanced and remained high, on a microsecond time scale, along with a slow microsecond time scale for recombination.<sup>[34]</sup> However, the performance may degrade if the mobility of the injected electron in the  $\text{TiO}_2$  layer is slower than that of perovskite. Therefore, careful design of oxide layers, taking into account this diffusion length and the mobility of the injected electrons, is important to achieve high efficiency.

Based upon the unique property of the perovskite, two typical structures can be constructed: a mesoscopic nanostructure and a planar structure. **Figure 4** shows schematic device structures and energetics. Charge separation by electron injection from perovskite to  $\text{TiO}_2$  is obvious in cases where perovskite dots are adsorbed onto the  $\text{TiO}_2$  surface.<sup>[8]</sup> In this case, the working principle is expected to be similar to dye-sensitized solid state solar cells. However, the working mechanism is different from dye-sensitized solar cells for both mesoscopic nanostructures with perovskite pore fillings (Figure 4a) and planar structures without a mesoporous  $\text{TiO}_2$  layer (Figure 4b), because of charge transport<sup>[30,31]</sup> and charge accumulation properties in the perovskite.<sup>[35]</sup> Carrier transport and recombination were compared for the mesoscopic structure and the planar structure; in this study, the former was lower in efficiency than the latter, and found to be the main factor affecting photovoltaic performance.<sup>[36]</sup> The results showed that the transport rate was the same but the recombination rate was higher for the mesoscopic structure. Since the resistances for transport and recombination are related to diffusion length, low performance was ascribed to a low diffusion length associated with a low recombination resistance, accelerating recombination. It was also

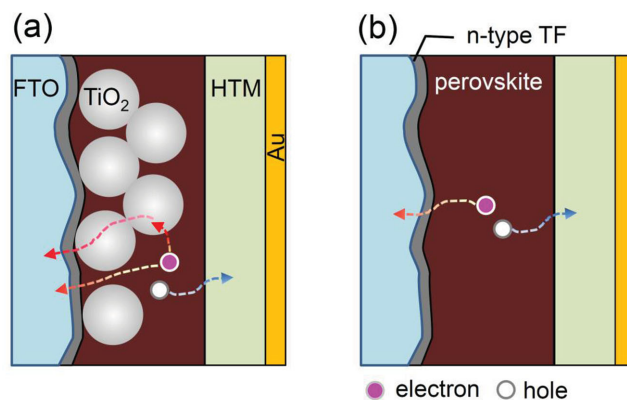


**Figure 4.** (a) Mesoscopic perovskite solar cell with mesoporous  $\text{TiO}_2$  layer and (b) planar structure without a mesoporous  $\text{TiO}_2$  layer. Thin film (TF) on fluorine doped tin oxide (FTO) is an n-type semiconductor. HTM stands for hole transporting material. In the mesoscopic structure, electrons can be collected directly and/or via  $\text{TiO}_2$  layer.

argued that the dominant transport pathway is the perovskite absorber, even in the mesoscopic structure. However, a different photovoltaic performance was observed from the comparative study on rutile and anatase  $\text{TiO}_2$  mesoporous films, which indicates that transport through the mesoporous  $\text{TiO}_2$  layer cannot be ruled out.<sup>[37]</sup> In the mesoscopic nanostructure, efforts have been made to facilitate charge transport by employing new nanomaterials such as ZnO nanorods, 3D- $\text{TiO}_2$  nanoparticles/ITO nanowire composites, and  $\text{TiO}_2$  nanoparticle/graphene composites.<sup>[38–40]</sup> The interface engineering of mesoscopic materials is one good way to control charge transport and recombination. Recently, an ultrathin MgO nanolayer was found to retard charge recombination between the electrons injected into  $\text{TiO}_2$  nanoparticles and the holes in perovskite materials.<sup>[41]</sup> This study demonstrates the importance of interface engineering for improving solar cell performance. Also, in the planar structure, the interface engineering impacts on the charge transport and recombination. Yang's group modified the ITO layer with polyethyleneimine ethoxylate (PEIE) to reduce the work function and increase the carrier density by doping yttrium into the  $\text{TiO}_2$  compact layer, thereby improving the electron transport channel in the planar structure perovskite solar cell.<sup>[42]</sup> Zhang et al. also inserted polyelectrolyte intermediate layers such as PEIE and P3TMAHT and achieved a high efficiency of 12%, which was attributed to the formation of surface dipoles, thereby reducing the work function of the subsequently deposited metal.<sup>[43]</sup> In the planar structure, there are two types of structures, i.e., planar and inverted planar structures. We will discuss this in more detail in Section 6.

Besides the two typical of perovskite solar cell structures depicted in Figure 4, an HTM-free structure is also possible because perovskite possesses hole transporting properties. In the case of hole transport material (HTM)-free perovskite solar cells, a thick perovskite layer with a smooth surface is needed to avoid forming shunt pathways as well as to form a good back contact to achieve high efficiency. The first demonstration of the HTM-free structure with an FTO/2D sheet  $\text{TiO}_2/\text{CH}_3\text{NH}_3\text{PbI}_3/\text{Au}$  configuration showed a PCE of 5.5%,<sup>[44]</sup> which was improved to 8% after replacing the  $\text{TiO}_2$  nanosheet with a thinner  $\text{TiO}_2$  nanoparticle film.<sup>[45]</sup> The photovoltaic performance of the HTM-free perovskite solar cell was dependent on the depletion layer width at the  $\text{TiO}_2\text{-CH}_3\text{NH}_3\text{PbI}_3$  junction, and enlargement of the width by increasing the depleted fraction of  $\text{TiO}_2$  led to a PCE of 10.85%.<sup>[46]</sup> A triple layer HTM-free perovskite solar cell, composed of a simple mesoscopic  $\text{TiO}_2/\text{ZrO}_2/\text{C}$  triple layer, has been exploited by Han et al.<sup>[47]</sup> The  $\text{ZrO}_2$  layer was found to block the flow of photogenerated electrons to the back contact, retarding recombination with the holes from the perovskite at the back contact. The cell achieved a certified power conversion efficiency of 12.8%.

The studied materials for perovskite solar cells are  $\text{CH}_3\text{NH}_3\text{PbI}_3$ ,  $\text{CH}_3\text{NH}_3\text{PbI}_{3-x}\text{Cl}_x$ ,  $\text{CH}_3\text{NH}_3\text{PbBr}_3$ ,  $\text{CH}_3\text{NH}_3\text{Pb(I}_{1-x}\text{Br}_x)_3$ ,  $\text{HC(NH}_2)_2\text{PbI}_3$ ,  $\text{HC(NH}_2)_2\text{Pb(I}_{1-x}\text{Br}_x)_3$  and  $\text{CH}_3\text{NH}_3\text{SnI}_3$ . In Table 1, the reported performances are summarized in terms of material and cell configuration. It is noted that most iodide perovskites exhibit an open-circuit

voltage over 1 V and bromide analogues demonstrate higher voltages than iodide ones. This is due to the fact that the bandgap of bromide perovskite is larger than that of iodide. HTM materials are also important for high efficiency perovskite solar cells, where the most studied HTM is spiro-MeOTAD, but polymertic HTMs such as the thiophene derivative P3HT and tryarylamine-based PTAA have also been tested. In addition, inorganic HTMs such as NiO, CuI, and CuSCN are confirmed to be suitable for perovskite solar cells.

## 4. Preparation Methods for High Efficiency Perovskite Solar Cells

### 4.1. Solution Process: One-Step Versus Two-Step Coatings

To deposit  $\text{CH}_3\text{NH}_3\text{PbI}_3$  perovskite on a substrate, two methods are available, that is, one-step and two-step coating methods. Perovskite forms either by spin-coating a mixed  $\text{CH}_3\text{NH}_3\text{I}$  and  $\text{PbI}_2$  solution (one-step coating) or by spin-coating  $\text{CH}_3\text{NH}_3\text{I}$  after coating with  $\text{PbI}_2$  (two-step coating). For the one-step coating method,  $\text{CH}_3\text{NH}_3\text{I}$  and  $\text{PbI}_2$  are dissolved in an appropriate solvent such as a polar aprotic solvent like *N,N*-dimethylformamide (DMF), gamma-butyrolactone (GBL), or dimethyl sulfoxide (DMSO), and this is used as a coating solution. Drying and annealing processes are followed by spin coating. For the two-step coating method,  $\text{PbI}_2$  solution is first coated on the substrate to form a  $\text{PbI}_2$  film and then a 2-propanol solution of  $\text{CH}_3\text{NH}_3\text{I}$  is spun on the  $\text{PbI}_2$  film. Figure 5 shows schematically the procedure for both the one-step and two-step spin-coating methods. In order to prepare high-quality perovskite films, it is important to adjust coating parameters such as spinning rate and time, temperature, solution wettability and viscosity, etc. Compared to one-step spin-coating, two-step spin-coating was found to exhibit better photovoltaic performance due to better morphology and interfaces,<sup>[79]</sup> which indicates that morphology control of perovskite film is crucial in achieving high-efficiency perovskite solar cells.

Perovskite prepared by the two-step coating method shows cuboid-like crystals, whereas the one-step method from the dimethyl acetamide (DMA) solution of  $\text{CH}_3\text{NH}_3\text{I}$  and  $\text{PbI}_2$  produced a shapeless morphology. It was found that the size of  $\text{CH}_3\text{NH}_3\text{PbI}_3$  was significantly altered by the concentration of  $\text{CH}_3\text{NH}_3\text{I}$  in the second deposition step.<sup>[56]</sup> When the concentration of the 2-propanol solution of  $\text{CH}_3\text{NH}_3\text{I}$  decreased from 0.063 M to 0.038 M, the average  $\text{CH}_3\text{NH}_3\text{PbI}_3$  crystal size increased from about 90 nm to about 700 nm, as shown in Figure 6.

In the case of the methylammonium lead iodide chloride ( $\text{CH}_3\text{NH}_3\text{PbI}_2\text{Cl}$ ) perovskite layer, whose diffusion length is 10 times longer than that of pure  $\text{CH}_3\text{NH}_3\text{PbI}_3$ , a single-step deposition process using a mixture of  $\text{CH}_3\text{NH}_3\text{I}$  and  $\text{PbCl}_2$  was adopted due to the poor solubility of  $\text{PbCl}_2$  in DMF. Recently, a two-step method was realized using a mixture of  $\text{PbCl}_2$  and  $\text{PbI}_2$  solution. The solubility of  $\text{PbCl}_2$  can be significantly increased in the presence of additives such as  $\text{PbI}_2$  due to the common ion effect. Wu et al. successfully dissolved

**Table 1.** Photovoltaic performance of perovskite solar cells depending on materials and cell configurations.  $J_{sc}$ ,  $V_{oc}$  and FF stand for short-circuit current density, open-circuit voltage, and fill factor, respectively. mp, bl and ETL represent mesoporous, blocking layer and extremely thin layer, respectively.

Materials	Cell configuration	$J_{sc}$ [mA/cm <sup>2</sup> ]	$V_{oc}$ [V]	FF	PCE [%]	Ref.
MAPbI <sub>3</sub>	mp-TiO <sub>2</sub> /MAPbI <sub>3</sub> /spiro-MeOTAD	17.6	0.888	0.62	9.7	[8]
	MAPbI <sub>3</sub> /PCBM	10.32	0.60	0.63	3.9	[48]
	ZnO nanorod/MAPbI <sub>3</sub> /spiro-MeOTAD	16.98	1.02	0.51	8.9	[49]
	mp-TiO <sub>2</sub> /MAPbI <sub>3</sub> /P3HT-MWNT	14.8	0.76	0.57	6.45	[50]
	rutile TiO <sub>2</sub> nanorod/MAPbI <sub>3</sub> /spiro-MeOTAD	15.6	0.955	0.63	9.4	[51]
	mp-TiO <sub>2</sub> /MAPbI <sub>3</sub> /PTAA	16.5	0.997	0.727	12	[52]
	mp-TiO <sub>2</sub> /MAPbI <sub>3</sub> (2-step)/spiro-MeOTAD	20	0.933	0.73	15	[53]
	mp-ZrO <sub>2</sub> /MAPbI <sub>3</sub> /spiro-MeOTAD	17.3	1.07	0.59	10.8	[54]
	mp-TiO <sub>2</sub> /MAPbI <sub>3</sub> (Toluene)/PTAA	19.58	1.105	0.76	16.46	[55]
	mp-TiO <sub>2</sub> /MAPbI <sub>3</sub> cuboid/spiro-MeOTAD	21.64	1.056	0.741	17.01	[56]
	ZnO nanorod/MAPbI <sub>3</sub> /spiro-MeOTAD	20.08	0.991	0.56	11.13	[38]
	NiO/MAPbI <sub>3</sub> /PCBM	13.24	1.040	0.69	9.51	[57]
	polyTPD/MAPbI <sub>3</sub> /PCBM	16.12	1.05	0.67	12.04	[58]
	ZnO (25 nm)/MAPbI <sub>3</sub> /spiro-MeOTAD	20.4	1.03	0.749	15.7	[59]
	NiO (45 nm)/MAPbI <sub>3</sub> /PCBM	16.27	0.882	0.635	9.11	[60]
	mp-TiO <sub>2</sub> /MAPbI <sub>3</sub> /CuSCN	19.7	1.016	0.62	12.4	[61]
	mp-TiO <sub>2</sub> /MAPbI <sub>3</sub> /CuI	17.8	0.55	0.62	6.0	[62]
MAPbI <sub>3-x</sub> Cl <sub>x</sub>	mp-Al <sub>2</sub> O <sub>3</sub> /MAPbI <sub>3-x</sub> Cl <sub>x</sub> /spiro-MeOTAD	17.8	0.98	0.63	10.9	[63]
	MAPbI <sub>3-x</sub> Cl <sub>x</sub> /P3HT	20.8	0.921	0.542	10.4	[64]
	(Al <sub>2</sub> O <sub>3</sub> + MAPbI <sub>3-x</sub> Cl <sub>x</sub> )/spiro-MeOTAD at T < 110 °C	12.78	0.925	0.61	7.16	[65]
	MAPbI <sub>3-x</sub> Cl <sub>x</sub> (evap.)/spiro-MeOTAD	21.5	1.07	0.67	15.4	[66]
	bl-Y:TiO <sub>2</sub> /MAPbI <sub>3-x</sub> Cl <sub>x</sub> (solution)/spiro-MeOTAD	22.75	1.13	0.75	19.3	[42]
MAPbBr <sub>3</sub>	mp-TiO <sub>2</sub> /MAPbBr <sub>3</sub> /PCBDTPP	4.47	1.16	0.59	3.04	[67]
	mp-Al <sub>2</sub> O <sub>3</sub> /MAPbBr <sub>3</sub> /PDI	1.08	1.30	0.4	0.56	[68]
	mp-TiO <sub>2</sub> /MAPbBr <sub>3</sub> /PIF8-TAA	6.1	1.40	0.79	6.7	[69]
	mp-Al <sub>2</sub> O <sub>3</sub> /MAPbBr <sub>3-x</sub> Cl <sub>x</sub> /CBP	4.0	1.50	0.46	2.7	[70]
MAPb(I,Br) <sub>3</sub>	mp-TiO <sub>2</sub> /MAPb(I <sub>0.8</sub> Br <sub>0.2</sub> ) <sub>3</sub> /PTAA	19.3	0.91	0.702	12.3	[71]
FAPbI <sub>3</sub>	mp-TiO <sub>2</sub> /FAPbI <sub>3</sub> /spiro-MeOTAD	6.45	0.97	0.687	4.3	[72]
	FAPbI <sub>3</sub> /spiro-MeOTAD	23.3	0.94	0.65	14.2	[73]
	mp-TiO <sub>2</sub> /FAPbI <sub>3</sub> /MAPbI <sub>3</sub> (ETL)/spiro-MeOTAD	20.97	1.032	0.74	16.01	[74]
	mp-TiO <sub>2</sub> /(MA <sub>0.6</sub> FA <sub>0.4</sub> )PbI <sub>3</sub> /spiro-MeOTAD	21.2	1.003	0.7	14.9	[75]
MASnX <sub>3</sub>	mp-TiO <sub>2</sub> /MASnI <sub>3</sub> /spiro-MeOTAD	16.8	0.88	0.42	6.4	[76]
	mp-TiO <sub>2</sub> /MASnI <sub>3</sub> /spiro-MeOTAD	16.3	0.68	0.48	5.23	[77]
	mp-TiO <sub>2</sub> /MASnIBr <sub>2</sub> /spiro-MeOTAD	12.30	0.82	0.57	5.73	[77]
MASn <sub>0.5</sub> Pb <sub>0.5</sub> I <sub>3</sub>	mp-TiO <sub>2</sub> /MASn <sub>x</sub> Pb <sub>(1-x)</sub> I <sub>3</sub> /P3HT	20.04	0.42	0.50	4.18	[78]

PbCl<sub>2</sub> salt in DMF with an addition of PbI<sub>2</sub> and then coated the mixture onto the mesoporous TiO<sub>2</sub> layer. After exposing it to CH<sub>3</sub>NH<sub>3</sub>I solution, finally a CH<sub>3</sub>NH<sub>3</sub>PbI<sub>3-x</sub>Cl<sub>x</sub> perovskite layer with controlled morphology was successfully obtained.<sup>[80]</sup>

It was found that the photovoltaic performance was strongly influenced by the CH<sub>3</sub>NH<sub>3</sub>I concentration, i.e., the crystal size of CH<sub>3</sub>NH<sub>3</sub>PbI<sub>3</sub>. In **Figure 7**, photovoltaic parameters are displayed with respect to CH<sub>3</sub>NH<sub>3</sub>I concentration. For the 0.038 M and 0.05 M cases, the average power conversion efficiencies

(PCE) were around 16.3%, whereas at high concentration of 0.063 M a lower PCE of 13.4% is obtained due to a lower photocurrent density and fill factor. It is noted that large crystals grown from low concentrations show higher  $J_{sc}$  than small ones grown from high concentrations, which is due to a higher light harvesting efficiency, as can be seen in **Figure 7e**, and a better charge-extraction ability, as measured by Photo-CELIV.<sup>[56,81]</sup> It is also noticed that  $V_{oc}$  would not increase with increasing crystal size.  $V_{oc}$  is higher for 0.050 M compared to those for 0.038 M and 0.063 M. It can be explained in connection with



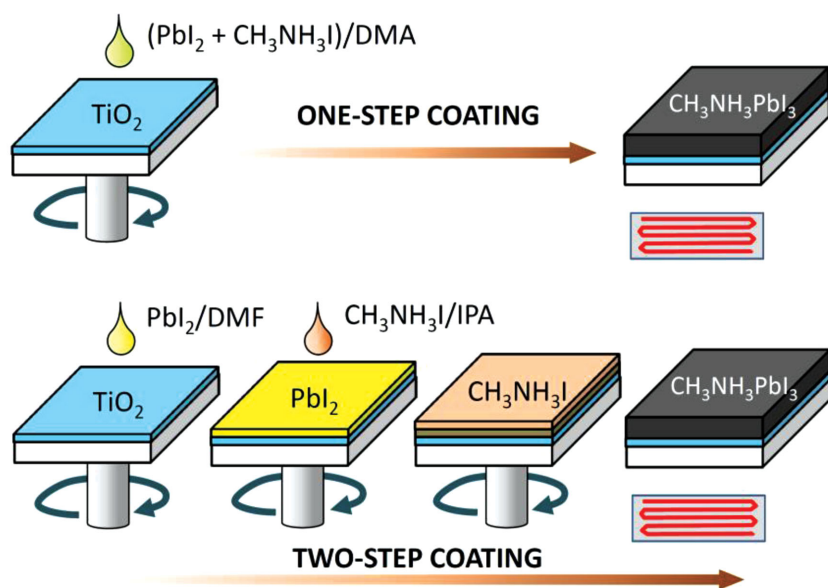


**Figure 5.** One-step and two-step coating procedures to deposit  $\text{CH}_3\text{NH}_3\text{PbI}_3$  perovskite films. DMA, DMF, and IPA represent dimethyl acetamide, dimethyl formamide, and isopropyl alcohol, respectively. Reproduced with permission.<sup>[79]</sup> Copyright 2014, AIP.

the Photo-CELIV results, that a change in  $V_{oc}$  correlates with the rate of charge-carrier extraction and recombination. A slow hole mobility with high charge extraction characteristics for 0.038 M or a fast hole mobility with low charge extraction characteristics for 0.063 M may not be beneficial to high  $V_{oc}$ : a slow hole mobility increases the probability of recombination. Thus, the lowest  $V_{oc}$  is observed for the large crystals prepared from the 0.038 M solution. Low charge extraction is likely to lead to not only low photocurrent but also a low Fermi level, which can affect  $V_{oc}$ . To realize high  $V_{oc}$  the intermediate size with fast mobility, i.e., minimized recombination, and high charge extraction, i.e., maximize the Fermi level, are required. The highest  $V_{oc}$  of 1.106 V is observed from the 0.050 M  $\text{CH}_3\text{NH}_3\text{I}$  solution.

Recently, solvent engineering enabled the control of morphology of the perovskite layer in solution processes to be comparable with the vacuum process. Cheng et al. reported that a single-step process was capable of fabricating flat and uniform perovskite films by immediately exposing the wet perovskite layer to chlorobenzene, which induced fast crystallization of the perovskite layer.<sup>[82]</sup> The role of chlorobenzene is to rapidly reduce the solubility of perovskite materials in the mixed DMF solvent, thereby promoting fast

nucleation and growth of crystals in the film. This technology allowed the reproducible fabrication of high-quality perovskite films. Seok's group also exploited a novel perovskite deposition technique using solvent engineering. They used a mixed solvent of  $\gamma$ -butyrolactone and dimethylsulphoxide (DMSO) followed by toluene drop-casting, which led to extremely uniform and dense perovskite layers.<sup>[55]</sup> The role of DMSO was to retard the rapid reaction between  $\text{PbI}_2$  and  $\text{CH}_3\text{NH}_3\text{I}$ , thereby forming a flat film containing an intermediate compound of  $\text{CH}_3\text{NH}_3\text{I-PbI}_2\text{-DMSO}$ . The toluene droplet quickly removed excess DMSO solvent from the wet film, which immediately quenched the constituents. Finally, a homogeneous flat perovskite layer was obtained after annealing at 100 °C. The efficiency of these devices was 16.2%, certified by the standardized method in a photovoltaics calibration laboratory. **Figure 8** shows an X-ray diffraction

(XRD) pattern of the intermediate and an SEM image of the resulting perovskite layer showing close-packed large grains.

The beauty of solvent engineering was recently verified in the two-step deposition process.<sup>[83]</sup> Since the rapid crystallization of  $\text{PbI}_2$  induces different crystal sizes on the hole-blocking layer, the resultant perovskite layer possesses inhomogeneity in grain size and stoichiometry. Han et al. used a strong coordinating solvent of DMSO to dissolve  $\text{PbI}_2$  and fabricated extremely flat amorphous  $\text{PbI}_2$  layers. Consequently, they were able to fabricate a uniform perovskite layer with a small distribution of crystal sizes and a flat surface morphology, which yielded highly reproducible perovskite solar cells with a high efficiency of 13.5%. Effects of additives such as  $\text{NH}_4\text{Cl}$  on the perovskite film were also characterized. Ding and Zuo recorded a 80.11% fill-factor using  $\text{NH}_4\text{Cl}$  additive, which was found to enhance the crystallinity and morphology of perovskite layer.<sup>[84]</sup>

#### 4.2. Vacuum Process

Perovskite films can be prepared by the thermal evaporation of chemicals. Co-evaporation of  $\text{CH}_3\text{NH}_3\text{I}$  and  $\text{PbCl}_2$

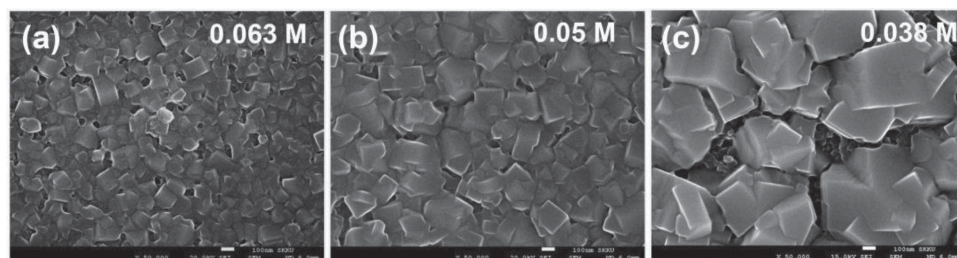


**Figure 6.** Scanning electron microscopy (SEM) images for  $\text{CH}_3\text{NH}_3\text{PbI}_3$  prepared from two-step spin-coating using (a) 0.063 M, (b) 0.05 M and (c) 0.038 M  $\text{CH}_3\text{NH}_3\text{I}$  solution. Scale bars represent 100 nm.



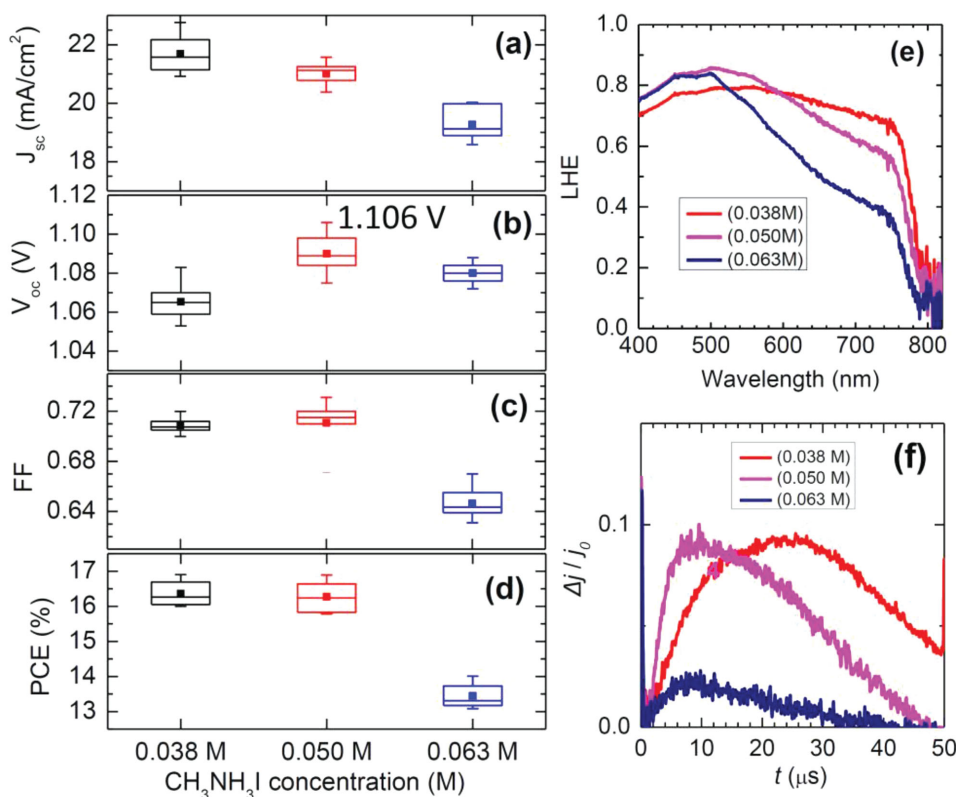


**Figure 7.** (a–d) Short-circuit current density ( $J_{sc}$ ), open-circuit voltage ( $V_{oc}$ ), fill factor (FF) and power conversion efficiency (PCE), depending on the  $\text{CH}_3\text{NH}_3\text{I}$  concentration. Error bars in each box represent minimum and maximum values and the middle line in the box represents the median value. Filled squares in the box represent mean values. (e) Light-harvesting efficiency spectra of the  $\text{CH}_3\text{NH}_3\text{PbI}_3$  films depending on  $\text{CH}_3\text{NH}_3\text{I}$  concentration. (f) Photo-CELIV transients recorded for the devices comprising  $\text{FTO}/\text{bI-Al}_2\text{O}_3/\text{mp-TiO}_2/\text{MAPbI}_3/\text{spiro-MeOTAD}/\text{Au}$ , depending on the  $\text{CH}_3\text{NH}_3\text{I}$  concentration. Reproduced with permission.<sup>[56]</sup> Copyright 2014, NPG.

leads to a  $\text{CH}_3\text{NH}_3\text{PbI}_3$  phase, and the uniformity of the film was much better than that of the solution-processed films, as shown in **Figure 9**.<sup>[66]</sup> The detailed evaporation process is as follows: A dual-source evaporation system with ceramic crucibles was installed in a  $\text{N}_2$ -filled glovebox.  $\text{CH}_3\text{NH}_3\text{I}$  and  $\text{PbCl}_2$  were co-evaporated from separate crucibles at  $10^{-5}$  mbar with an as-deposited molar ratio of 4:1. It was observed that a dark reddish-brown colour appeared immediately after evaporation. Annealing was performed to crystallize the as-deposited perovskite.<sup>[66]</sup> The thin perovskite film was prepared by co-evaporation using  $\text{CH}_3\text{NH}_3\text{I}$  and  $\text{PbI}_2$ , in which the crucible containing  $\text{CH}_3\text{NH}_3\text{I}$  was heated to 70 °C and the other containing  $\text{PbI}_2$  was heated to 250 °C at  $10^{-6}$  mbar.<sup>[58]</sup> The vacuum deposition method seems to be better for thickness control, compared to the solution process.

Thermal evaporation requires high vacuum, which restricts cost effectiveness and mass production. To overcome this problem, a vapor-assisted solution process (VASP), which grows perovskite films via in situ reactions of as-deposited films of  $\text{PbI}_2$  with  $\text{CH}_3\text{NH}_3\text{I}$  vapor, was developed.<sup>[85]</sup> The perovskite film prepared via this method showed a well-defined grain structure with grain sizes up to the microscale, full surface coverage, and small surface roughness.

## 5. Photoluminescence and Polarization Characteristics

One of the important optical properties when studying photovoltaic materials is photoluminescence (PL), which provides several pieces of information including bandgap, chemical purity, and charge separation. **When semiconducting materials absorb photons, electronic excitations occur and then these excitations relax to return to the ground state.** Radiative relaxation is called PL. When measuring solid thin films like the organometal halide perovskite films, in contrast to solution samples, careful measurements should be carried out because the angular distribution of the emitted light is highly sensitive to the refractive index of the material and to the orientation of the emitting dipoles within the film.<sup>[86]</sup> To minimize the angular distribution, an integrating sphere is recommended to get the absolute PL efficiency of a solid thin film.<sup>[87]</sup> However, a conventional set-up may be allowed for comparative studies or relative PL efficiencies. The PL spectra of various organometal halide perovskite materials are collected in **Figure 10**. Lead-based  $\text{CH}_3\text{NH}_3\text{PbI}_3$  and  $\text{HC}(\text{NH}_2)_2\text{PbI}_3$  show PL values between 750 and 850 nm, where the maximum PL of  $\text{HC}(\text{NH}_2)_2\text{PbI}_3$  at around 800 nm is red-shifted compared to that of  $\text{CH}_3\text{NH}_3\text{PbI}_3$  at around 775 nm (Figure 10a).<sup>[19]</sup>  $\text{CH}_3\text{NH}_3\text{SnI}_3$  shows red-shifts of

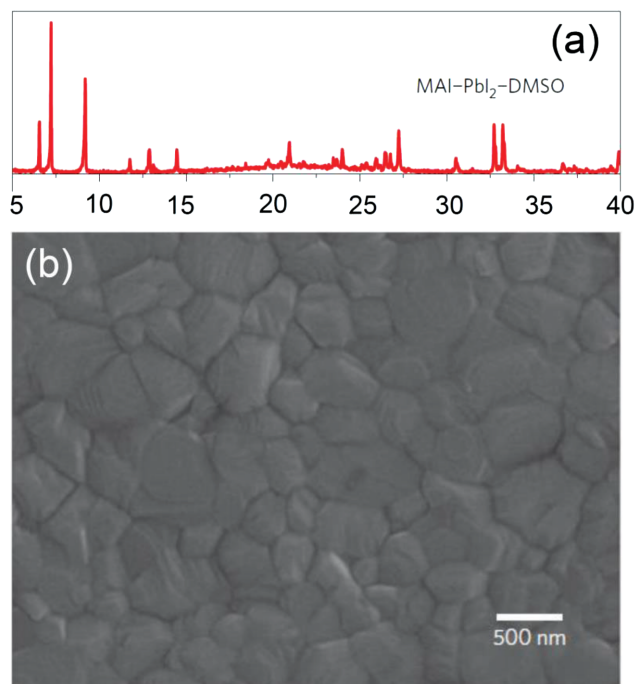


**Figure 8.** (a) X-ray diffraction pattern of a MAI-PbI<sub>2</sub>-DMSO intermediate phase formed by toluene treatment on the film formed by spin-coating of MAI-PbI<sub>2</sub>-DMSO-GBL solution. (b) SEM image of the resulting perovskite film via the intermediate phase. Reproduced with permission.<sup>[55]</sup> Copyright 2014, NPG.

more than 180 nm and broader PL peaks compared to its lead analogue, as can be seen in Figure 10b,<sup>[76]</sup> which is due to its smaller bandgap. Systematic evolution in PL peak shifts is observed upon substitution of methylammonium ( $\lambda = 776$  nm) for formamidinium ( $\lambda = 776$  nm) in lead iodide perovskite (Figure 10c).<sup>[75]</sup> It is noted that PL peaks are broadened upon increasing the formamidinium ratio, which indicates the formation of a solid solution of methylammonium and formamidinium in the perovskite lattice.<sup>[75]</sup> In Figure 10d, a gradual blue-shift in PL peaks is observed upon the substitution of iodide for bromide in lead halide perovskite, due to a gradual increase in the bandgap.<sup>[88]</sup> The sharp

emission peak for pure iodide broadens as the bromide ratio increases or vice versa, which is indicative of the formation of solid solutions of iodide and bromide in the lattice.

PL quenching measurements are a fast and facile way to investigate charge separation. In the case where perovskite is in contact with an electron acceptor (n-type quencher) or hole acceptor (p-type quencher), PL intensity will be decreased compared to the isolated state due to charge separation by electron or hole injection. From the change in PL intensity, one can evaluate the degree and effectiveness of charge separation. **Figure 11** shows the change in PL intensity for the CH<sub>3</sub>NH<sub>3</sub>PbI<sub>3</sub> or CH<sub>3</sub>NH<sub>3</sub>PbI<sub>3-x</sub>Cl<sub>x</sub> perovskites in the absence and presence of n-type or p-type quenchers. A significant decrease in PL intensity is observed when both perovskite materials are in contact with electron-accepting PCBM and hole accepting spiro-MeOTAD, as shown in Figures 11a and b,<sup>[30,31]</sup> which is attributed to the injection of electrons and holes. It is also obvious that electrons are injected into mesoporous TiO<sub>2</sub> layers but not into Al<sub>2</sub>O<sub>3</sub>, because of the higher conduction band position (Figure 11c). However, contrary to the case of spiro-MeOTAD, PL is hardly quenched by PTAA. This suggests that CH<sub>3</sub>NH<sub>3</sub>PbI<sub>3</sub> can act as a hole-conducting layer.<sup>[52]</sup> In the presence of inorganic hole conductors such as NiO and CuSCN, charge separation occurs well, as evidenced by significant PL quenching shown in Figure 11d, where CuSCN is superior to NiO in terms of charge-separation efficiency.<sup>[89]</sup> Investigations of PL quenching are thus a useful tool to study charge separation and to get information on interfacial contacts.

Impedance spectroscopic studies on solid-state perovskite solar cells give important insights into carrier transport, recombination, and diffusion length. According to impedance measurements for two different planar and mesoscopic perovskite solar cell structures, it was found that carrier conductivity in both devices was similar but recombination resistance was slightly higher for the planar cell than for the mesoscopic one.<sup>[89]</sup> In addition, diffusion length, calculated based on impedance results, was longer for CH<sub>3</sub>NH<sub>3</sub>PbI<sub>3-x</sub>Cl<sub>x</sub> in the planar structure than for CH<sub>3</sub>NH<sub>3</sub>PbI<sub>3</sub> in the mesoscopic structure, which is consistent with the diffusion length estimated from time-resolved PL.<sup>[90]</sup> The impedance result

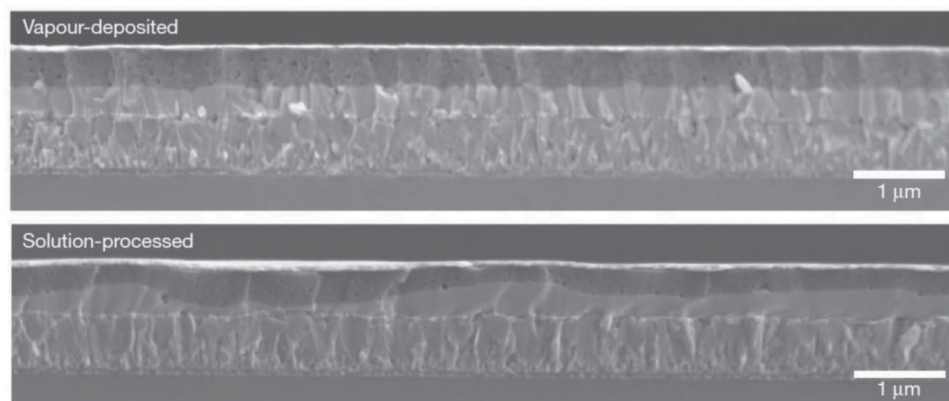


**Figure 9.** Comparison of the perovskite film uniformity between vapor-deposition and solution-process methods. Reproduced with permission.<sup>[66]</sup> Copyright 2013, NPG.

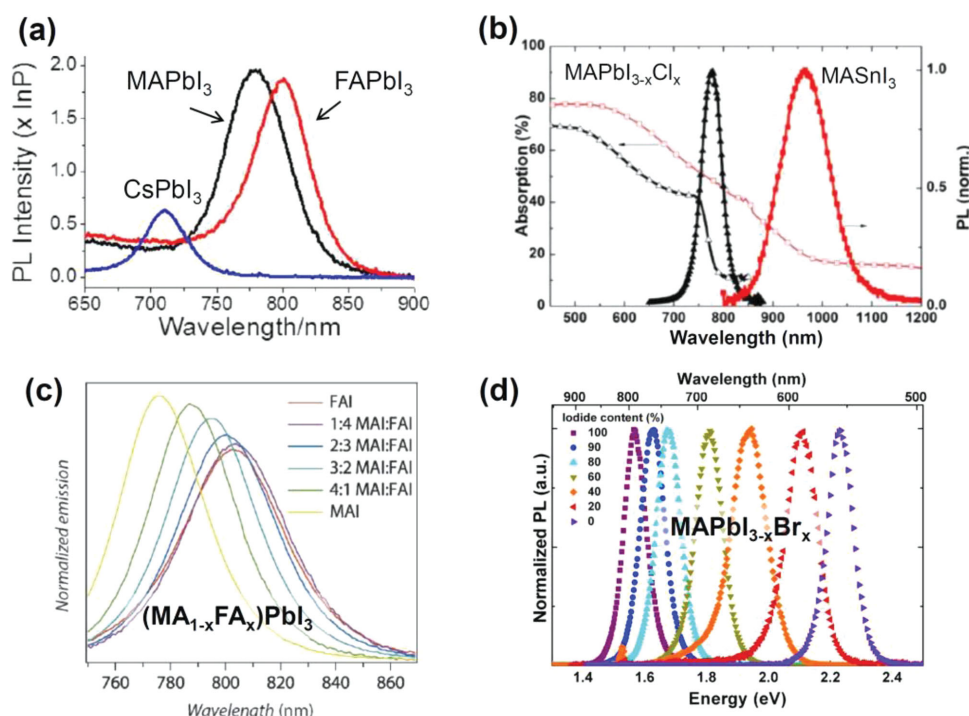


**Figure 10.** Photoluminescence (PL) characteristics of various organometal halide perovskite materials including (a) lead iodides (Reproduced with permission.<sup>[19]</sup> Copyright 2013, NPG.), (b) tin iodide (Reproduced with permission.<sup>[75]</sup> Copyright 2014, Wiley.), (c) methylammonium and formamidinium mixed lead iodides (Reproduced with permission.<sup>[76]</sup> Copyright 2014, RSC), and (d) iodide and bromide mixed halides (Reproduced with permission.<sup>[88]</sup> Copyright 2014, ACS.). PL spectra were obtained by photoexcitation at 532 nm for (a), 500 nm for (b), 460 nm for (c) and 400 nm (3.1 eV) for (d).

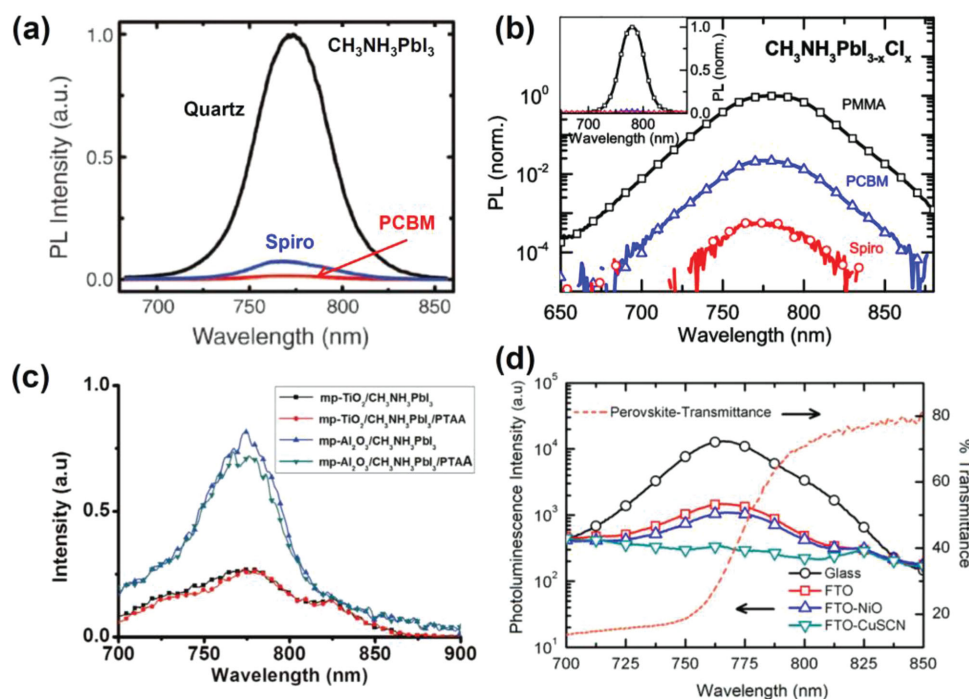


**Figure 11.** PL quenching behaviors for: (a) CH<sub>3</sub>NH<sub>3</sub>PbI<sub>3</sub>/spiro-MeOTAD system with excitation at 600 nm. Reproduced with permission.<sup>[30]</sup> Copyright 2014, AAAS. (b) CH<sub>3</sub>NH<sub>3</sub>PbI<sub>3-1-x</sub>Cl<sub>x</sub>/spiro-MeOTAD system with excitation at 507 nm. Reproduced with permission.<sup>[31]</sup> Copyright 2014, AAAS. (c) CH<sub>3</sub>NH<sub>3</sub>PbI<sub>3</sub>/PTAA system with excitation at 600 nm. Reproduced with permission.<sup>[52]</sup> Copyright 2013, NPG. (d) CH<sub>3</sub>NH<sub>3</sub>PbI<sub>3-1-x</sub>Cl<sub>x</sub>/inorganic HTM system with excitation at 530 nm. Reproduced with permission.<sup>[89]</sup> Copyright 2014, ACS. Note that (a) and (c) are linear scales but (b) and (d) are log scales. Inset in (b) shows a linear scale.



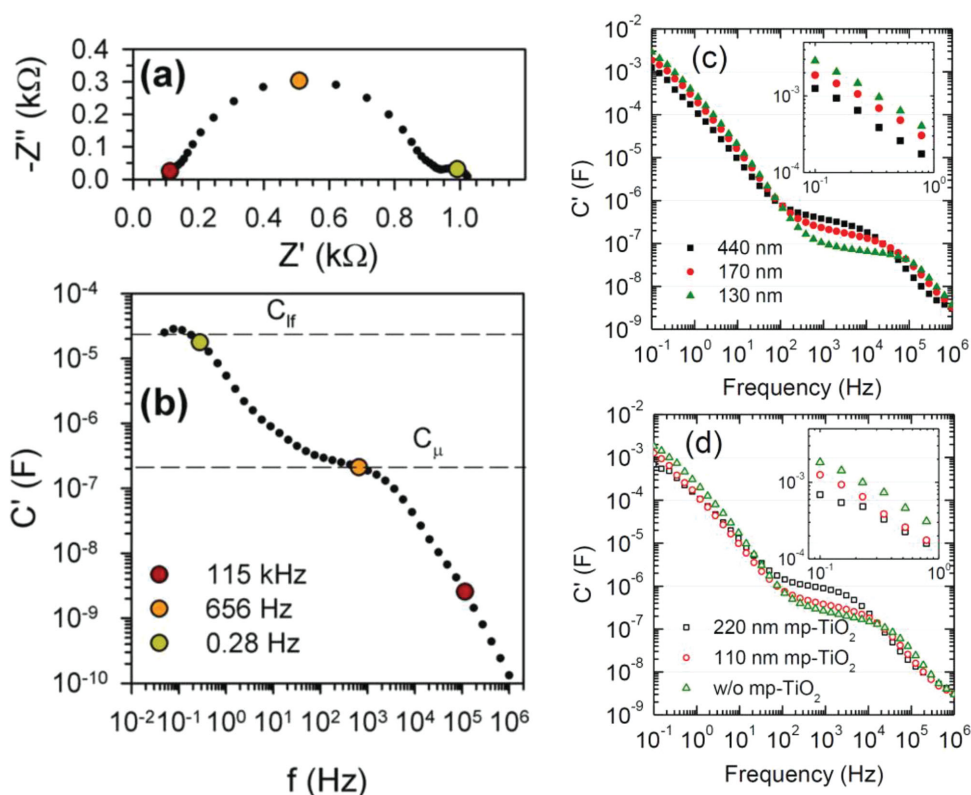


**Figure 12.** (a) A typical impedance plot (imaginary part of the impedance  $Z''$  versus the real part  $Z'$ ) and (b) Bode plot of the real part of the capacitance  $C'$  obtained under dark conditions at 0.9 V applied DC bias. Three frequencies are highlighted to distinguish low, intermediate, and high-frequency regions. Reproduced with permission.<sup>[91]</sup> Copyright 2014, ACS. Bode plots of the real part of the capacitance obtained from impedance spectroscopy measured under one sun illumination at the applied voltage of 0.8 V for the devices (c) with different  $\text{CH}_3\text{NH}_3\text{PbI}_3$  crystal size and (d) in the absence and presence of a  $\text{mp-TiO}_2$  layer. Inset shows the capacitance at low frequencies (10<sup>-1</sup> to 10<sup>2</sup> Hz). Reproduced with permission.<sup>[93]</sup> Copyright 2014, ACS.

indicates that the perovskite light absorber plays a central role in perovskite solar cell performance, regardless of differences between the samples in terms of preparation method and cell configuration. Moreover, impedance measurements can provide information on the polarization of the perovskite material. As can be seen in **Figure 12**, there are three arcs in a complex impedance plot at low, intermediate, and high frequencies. The high-frequency arc is associated with selective contacts, the intermediate-frequency arc is associated with the chemical capacitance, and the low-frequency arc is related to the polarization created by aligning dipoles or dipolar domains to the external electrical field.<sup>[91]</sup> The basis for the interpretation of polarization being at the low-frequency capacitance is because the rearrangement of the overall orientation in response to any external perturbation will occur over slow time dynamics.<sup>[91]</sup> The polarization phenomenon in perovskite materials probably causes current-voltage hysteresis. Anomalous I-V hysteresis, differences in I-V curves depending on scan direction, was observed from  $\text{CH}_3\text{NH}_3\text{PbI}_{3-x}\text{Cl}_x$ <sup>[92]</sup> and  $\text{CH}_3\text{NH}_3\text{PbI}_3$ .<sup>[93]</sup> Such I-V hysteresis was found to be strongly dependent on perovskite crystal size and the presence of a  $\text{mp-TiO}_2$  film, where large-sized perovskite and the presence of  $\text{mp-TiO}_2$  would suppress I-V hysteresis.<sup>[93]</sup> The degree of I-V hysteresis was found to correlate with low-frequency capacitance, that is, the low-frequency capacitance decreased as the crystal size of

$\text{CH}_3\text{NH}_3\text{PbI}_3$  increased, and also in the presence of  $\text{mp-TiO}_2$  (Figures 12c and d), which indicates that polarizability is closely related to I-V hysteresis and large crystals and/or the inclusion of  $\text{mp-TiO}_2$  is beneficial to its suppression.

## 6. Perovskite Suitable for Flexible Solar Cells

Flexible thin film solar cells are open to various potential applications such as portable electronic chargers, bendable display devices, and wearable electronic textiles due to their light weight, bendability, and easy shape changeability.<sup>[94,95]</sup> Perovskite solar cells are fairly attractive as flexible solar cells due to the low temperature processing (below ~150 °C), all-solid-state nature of the thin films, and high efficiency. Flexible perovskite solar cells are now at a beginning stage, which implies that there is much room for innovation.

Flexible perovskite solar cells have been realized by employing two types of structures, i.e., n-i-p and p-i-n junctions, containing electron transport materials (ETM)/perovskite/HTM and HTM/perovskite/ETM architectures, respectively. Since conventional process for the fabrication of ETM such as a  $\text{TiO}_2$  compact layer needs a high temperature (over ~400 °C), most flexible perovskite solar cells on ITO-coated poly(ethylene terephthalate) (PET) substrates

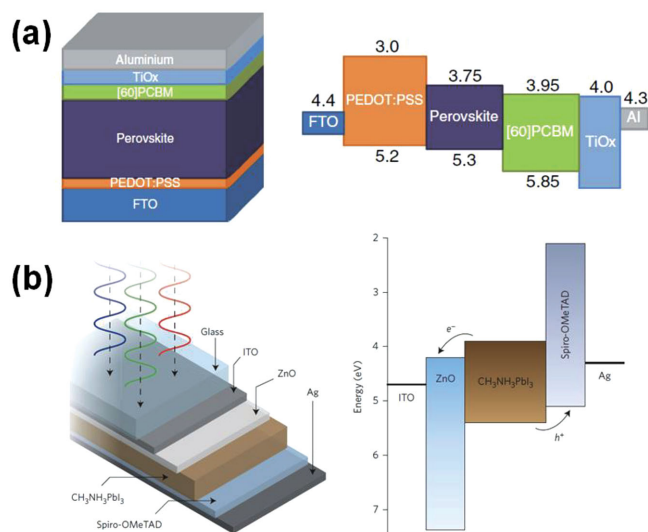


**Figure 13.** (a) A typical p-i-n device configuration and schematic band diagram of the fabricated solar cell and (b) a typical n-i-p device configuration and schematic band diagram of the fabricated solar cell. Reproduced with permission.<sup>[96,59]</sup> Copyright 2013,2014 NPG.

have adopted p-i-n structures (or inverted planar structures) composed of PEDOT:PSS/perovskite/PCBM architectures (**Figure 13(a)**).<sup>[96–98]</sup> These materials are able to be deposited at a low temperature (below 150 °C), which is suitable for the fabrication of flexible solar cells based on PET substrates. Also, flexible perovskite solar cells composed of n-i-p structures (planar structures) were realized by depositing ZnO ETM at a low temperature (Figure 13(b)).<sup>[42,54]</sup> ZnO nano-materials have also been known to be deposited at below 150 °C. Kelly et al. reported an n-i-p structured flexible

perovskite solar cell whose power conversion efficiency (PCE) was 10.2%.<sup>[59]</sup>

Recently, a high efficiency flexible perovskite solar cell whose PCE is over 12% was created by employing a TiO<sub>x</sub> compact layer deposited using atomic layer deposition (ALD) (**Figure 14(a)**).<sup>[99]</sup> As shown in Figure 14(b), this solar cell shows superior mechanical endurance properties, i.e., its energy conversion efficiency does not change after 1000 cycles of bending tests under conditions of a bending radius of 10 mm, demonstrating that the flexible perovskite solar cells are potentially usable as a power solution for future wearable devices.

## 7. Long-Term Stability

The long-term stability of perovskite solar cells is another big issue. The degradation mechanism of perovskite materials is not clearly understood. An understanding of the degradation mechanism will be helpful to enhance the long-term stability, which will be a significant criterion for the commercialization of perovskite solar cells. Recently, remarkable efforts on improving long-term stability have been made, although it has been not under active research. Snaith's group employed P3HT/single-walled carbon nanotubes (SWCNT)-PMMA double layer as a HTM.<sup>[100]</sup> The perovskite solar cell demonstrated remarkable thermal and moisture stability. The P3HT polymer-based HTM showed superior temperature stability compared with the single-molecule based spiro-OMeTAD. The PCE dropped to 20% of initial efficiency after heating the cell at 80 °C for 20 min, which exhibited a temperature coefficient of  $\sim 0.33\%/^{\circ}\text{C}$ . This result is similar to that of the copper indium gallium (di)selenide (CIGS) solar cell. The

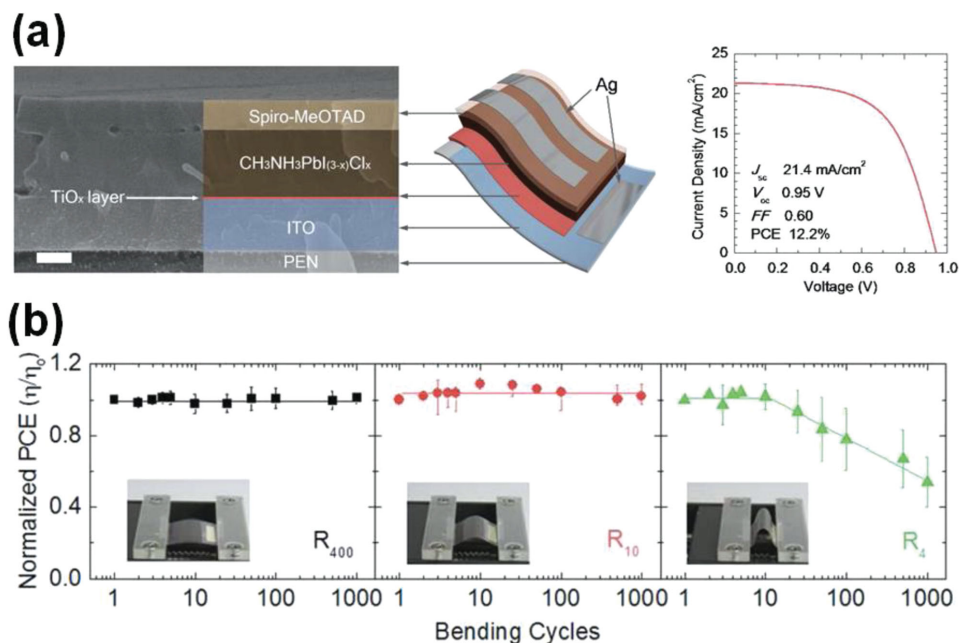


**Figure 14.** (a) Cross-sectional SEM image of inorganic-organic halide perovskite planar heterojunction flexible solar cell and schematic of flexible device structure. Scale bar: 200 nm and I-V characteristics measured under the simulated solar light (100 mW/cm<sup>2</sup> AM 1.5G) and (b) normalized PCE of flexible perovskite devices as a function of bending cycles with different radii of 400, 10, and 4 mm. Inset show the real images taken during the bending tests. Reproduced with permission.<sup>[99]</sup> Copyright 2014, RSC.

hydrophobic PMMA showed a significant waterproof property, which retarded decomposition of the perovskite layer by water vapor. Han et al. reported remarkable progress regarding this stability issue:<sup>[47]</sup> they fabricated a HTM-free and triple layer-based perovskite solar cell, composed of a simple mesoscopic  $\text{TiO}_2/\text{ZrO}_2/\text{C}$  triple layer as a scaffold to host the perovskite absorber. The 10  $\mu\text{m}$  thick carbon back contact layer played an important role in resistance to water. This cell exhibited excellent stability under AM 1.5 conditions over 1008 h.

## 8. Summary and Outlook

In this review article, we have given an overview of the historical progress in perovskite solar cells and revisited the fundamentals of organometal halide perovskite materials from a viewpoint of optical absorption and charge transport properties. Photoluminescence and impedance analysis were described to be important tools which characterized the charge separation, carrier transport, recombination, and diffusion length in perovskite solar cells. Moreover, the correlation between dielectric properties and the chemical bonding nature in ionic crystals with molecular organic ions was also discussed, which is also of great importance to understand the photovoltaic properties of organometal halide perovskite materials. Fabrication methods, including solution and vacuum processes, were shown to influence crystal growth and the morphologies of perovskite materials, thereby impacting on the resultant energy conversion efficiency. Also, recent progress underlying solution engineering exhibited the capability of controlling the morphology of perovskite materials for maximizing the energy conversion efficiency. In particular, the potential of perovskite solar cells for use as flexible solar cells was discussed in terms of low temperature processing (below  $\sim 150^\circ\text{C}$ ), all-solid-state thin film nature, and high efficiency. The flexible perovskite solar cell showed an extraordinary bending durable property, fairly suitable for being used as a power solution for future wearable devices.

The high-efficiency and cost-effective materials and processes for perovskite solar cells make them economically viable for commercialization. Theoretically calculated maximum efficiencies for perovskite solar cell are reported by Yan et al.<sup>[101]</sup> Based on considerations of the optical absorption coefficient and thickness of the light absorber, the theoretical maximum efficiency for a 1  $\mu\text{m}$ -thick perovskite solar cell composed of  $\text{CH}_3\text{NH}_3\text{PbI}_3$  (phase with  $P_{m\bar{3}m}$  symmetry) is 26%, which is much higher than the efficiency of a GaAs solar cell with the same thickness. This result indicates that the perovskite solar cells are economically viable from a viewpoint of efficiency. However, commercialization is still challenging because of (1) the toxicity of Pb atoms, (2) long-term stability, and (3) cost-effectiveness. So far, the champion cells have been based on Pb-based perovskite materials. However, the utilization of Pb-based materials has been restricted due to their intrinsic toxicity. Future research directions are going to be finding Pb-free light-absorbing materials. Protection technology, in order not to release Pb from the Pb-based perovskite solar cell device, will be important

issue, which may learn from the CdTe solar cell industry. So far, 1000 h operation time has been guaranteed. However, this result is not enough to commercialize perovskite solar cells. Understanding the degradation mechanism as well as exploiting new materials and external encapsulation technologies should realize a more-than-20-years operation lifetime. The cost-effectiveness for materials and processes is a significant issue. The high throughput with reproducible materials and processes should be developed. Moreover, mechanical functionalities such as flexibility and stretchable properties will lead to making the perovskite solar cells more economically viable.

## Acknowledgments

This work was supported by the National Research Foundation of Korea (NRF) grants funded by the Ministry of Science, ICT & Future Planning (MSIP) of Korea under contracts No. NRF-2010-0014992, NRF-2012M1A2A2671721, 2012M3A7B4049986 (Nano Material Technology Development Program) and NRF-2012M3A6A7054861 (Global Frontier R&D Program on Center for Multiscale Energy System).

- [1] D. Weber, *Z. Naturforsch.* **1978**, *33b*, 1443.
- [2] D. Weber, *Z. Naturforsch.* **1978**, *33b*, 862.
- [3] D. B. Mitzi, C. A. Feild, W. T. A. Harrison, A. M. Guloy, *Nature* **1994**, *369*, 467.
- [4] A. Kojima, K. Teshima, Y. Shirai, T. Miyasaka, *J. Am. Chem. Soc.* **2009**, *131*, 6050.
- [5] A. Hagfeldt, G. Boschloo, L. Sun, L. Kloo, H. Pettersson, *Chem. Rev.* **2010**, *110*, 6595.
- [6] G. Chen, J. Seo, C. Yang, P. N. Prasad, *Chem. Soc. Rev.* **2013**, *42*, 8304.
- [7] J.-H. Im, C.-R. Lee, J.-W. Lee, S.-W. Park, N.-G. Park, *Nanoscale* **2011**, *3*, 4088.
- [8] H.-S. Kim, C.-R. Lee, J.-H. Im, K.-B. Lee, T. Moehl, A. Marchioro, S.-J. Moon, R. Humphry-Baker, J.-H. Yum, J. E. Moser, M. Grätzel, N.-G. Park, *Sci. Rep.* **2012**, *2*, 591.
- [9] F. G. Fumi, M. P. Tosi, *J. Chem. Phys.* **1960**, *33*, 1.
- [10] Y. Sakamoto, *J. Chem. Phys.* **1958**, *28*, 164.
- [11] D. Quane, *J. Chem. Educ.* **1970**, *47*, 396.
- [12] L. L. Hench, J. K. West *Principles of Electronic Ceramics* 1st Ed., A Wiley-Interscience Publication, New York **1990**, p.193.
- [13] W.-S. Xia, L.-X. Li, P.-F. Ning, Q.-W. Liao, *J. Am. Ceramic Soc.* **2012**, *95*, 2587.
- [14] R. E. Wasylshen, O. Knop, J. B. Macdonald, *Solid State Commun.* **1985**, *56*, 581.
- [15] A. Poglitsch, D. Weber, *J. Chem. Phys.* **1987**, *87*, 6373.
- [16] N. Onoda-Yamamura, *Doctoral Thesis*, Osaka University, **1990**.
- [17] W. Geng, L. Zhang, Y.-N. Zhang, W.-M. Lau, L.-M. Liu, *J. Phys. Chem. C* **2014**, DOI: 10.1021/jp504951h.
- [18] S. D. Wolf, J. Holovsky, S.-J. Moon, P. Löper, B. Niesen, M. Ledinsky, F.-J. Haug, J.-H. Yum, C. Ballif, *J. Phys. Chem. Lett.* **2014**, *5*, 1035.
- [19] C. C. Stoumpos, C. D. Malliakas, M. G. Kanatzidis, *Inorg. Chem.* **2013**, *52*, 9019.
- [20] F. Hao, C. C. Stoumpos, R. P. H. Chang, M. G. Kanatzidis, *J. Am. Chem. Soc.* **2014**, *136*, 8094.
- [21] T. Umebayashi, K. Asai, T. Kondo, A. Nakao, *Phys. Rev. B* **2003**, *67*, 155405.



- [22] E. Mosconi, A. Amat, M. K. Nazeeruddin, M. Grätzel, F. D. Angelis, *J. Phys. Chem. C* **2013**, *117*, 13902.
- [23] P. Umari, E. Mosconi, F. D. Angelis, *Sci. Rep.* **2014**, *4*, 4467.
- [24] N. Onoda-Yamamuro, T. Matsuo, H. Suga, *J. Phys. Chem. Solids* **1990**, *51*, 1383.
- [25] N. Onoda-Yamamuro, T. Matsuo, H. Suga, *J. Phys. Chem. Solids* **1992**, *53*, 935.
- [26] E. J. Juarez-Perez, R. S. Sanchez, L. Badia, G. Garcia-Belmonte, Y. S. Kang, I. Mora-Sero, J. Bisquert, *J. Phys. Chem. Lett.* **2014**, *5*, 2390.
- [27] *Principles of Electronic Ceramics*, Wiley, NY, USA, **1990**.
- [28] K. Yamada, T. Matsui, T. Tsuritani, T. Okuda, S. Ichiba, *Z. Naturforsch.* **1990**, *45a*, 307.
- [29] K. Yamada, H. Kawaguchi, T. Matsui, T. Okuda, S. Ichiba, *Bull. Chem. Soc. Jpn.* **1990**, *63*, 3521.
- [30] G. Xing, N. Mathews, S. Sun, S. S. Lim, Y. M. Lam, M. Grätzel, S. Mhaisalkar, T. C. Sum, *Science* **2013**, *342*, 344.
- [31] S. D. Stranks, G. E. Eperon, G. Grancini, C. Menelaou, M. J. P. Alcocer, T. Leijtens, L. M. Herz, A. Petrozza, H. J. Snaith, *Science* **2013**, *342*, 341.
- [32] E. Edri, S. Kirmayer, A. Henning, S. Mukhopadhyay, K. Gartsman, Y. Rosenwaks, G. Hodes, D. Cahen, *Nano Lett.* **2014**, *14*, 1000.
- [33] Y. Zhao, A. M. Nardes, K. Zhu, *J. Phys. Chem. Lett.* **2014**, *5*, 490.
- [34] C. S. Ponseca Jr., T. J. Savenije, M. Abdellah, K. Zheng, A. Yartsev, T. Pascher, T. Harlang, P. Chabera, T. Pullerits, A. Stepanov, J.-P. Wolf, V. Sundstrom, *J. Am. Chem. Soc.* **2014**, *136*, 5189.
- [35] H.-S. Kim, I. Mora-Sero, V. Gonzalez-Pedro, F. Fabregat-Santiago, E. J. Juarez-Perez, N.-G. Park, J. Bisquert, *Nat. Commun.* **2013**, *4*, 2242.
- [36] V. Gonzalez-Pedro, E. J. Juarez-Perez, W.-S. Arsyad, E. M. Barea, F. Fabregat-Santiago, I. Mora-Sero, J. Bisquert, *Nano Lett.* **2014**, dx.doi.org/10.1021/nl404252e.
- [37] J.-W. Lee, T.-Y. Lee, P. J. Yoo, M. Grätzel, S. Mhaisalkar, N.-G. Park, *J. Mater. Chem. A* **2014**, *2*, 9251.
- [38] D.-Y. Son, J.-H. Im, H.-S. Kim, N.-G. Park, *J. Phys. Chem. C* **2014**, *118*, 16567.
- [39] G. S. Han, S. Lee, J. H. Noh, H. S. Chung, J. H. Park, B. S. Swain, J.-H. Im, N.-G. Park, H. S. Jung, *Nanoscale* **2014**, *6*, 6127.
- [40] J. T.-W. Wang, J. M. Ball, E. M. Barea, A. Abate, J. A. Alexander-Webber, J. Huang, M. Saliba, I. Mora-Sero, J. Bisquert, H. J. Snaith, R. J. Nicholas, *Nano Lett.* **2014**, *14*, 724.
- [41] G. S. Han, H. S. Chung, B. J. Kim, D. H. Kim, J. W. Lee, B. S. Swain, K. Mahmood, J. S. Yu, N.-G. Park, J. H. Lee, H. S. Jung, *J. Mater. Chem. A* **2014**, DOI: 10.1039/C4TA03684K.
- [42] H. Zhou, Q. Chen, G. Li, S. Luo, T.-B. Song, H.-S. Duan, Z. Hong, J. You, Y. Liu, Y. Yang, *Science* **2014**, *345*, 542.
- [43] H. Zhang, H. Azimi, Y. Hou, T. Ameri, T. Przybilla, E. Spiecker, M. Kraft, U. Scherf, C. J. Brabec, *Chem. Mater.* **2014**, *26*, 5190.
- [44] L. Etgar, P. Gao, Z. Xue, Q. Peng, A. K. Chandiran, B. Liu, M. K. Nazeeruddin, M. Grätzel, *J. Am. Chem. Soc.* **2012**, *134*, 17396.
- [45] W. A. Laban, L. Etgar, *Energy Environ. Sci.* **2013**, *6*, 3249.
- [46] S. Aharon, S. Gamliel, B. E. Cohen, L. Etgar, *Chem. Chem. Phys.* **2014**, *16*, 10512.
- [47] A. Mei, X. Li, L. Liu, Z. Ku, T. Liu, Y. Rong, M. Xu, M. Hu, J. Chen, Y. Yang, M. Grätzel, H. Han, *Science* **2014**, *345*, 295.
- [48] J.-Y. Jeng, Y.-F. Chiang, M.-H. Lee, S.-R. Peng, T.-F. Guo, P. Chen, T.-C. Wen, *Adv. Mater.* **2013**, *25*, 3727.
- [49] M. H. Kumar, N. Yantara, S. Dharani, M. Graetzel, S. Mhaisalkar, P. P. Boix, N. Mathews, *Chem. Commun.* **2013**, *49*, 11089.
- [50] H. Chen, X. Pan, W. Liu, M. Cai, D. Kou, Z. Huo, X. Fang, S. Dai, *Chem. Commun.* **2013**, *49*, 7277.
- [51] H.-S. Kim, J.-W. Lee, N. Yantara, P. P. Boix, S. A. Kulkarni, S. Mhaisalkar, M. Grätzel, N.-G. Park, *Nano Lett.* **2013**, *13*, 2412.
- [52] J. H. Heo, S. H. Im, J. H. Noh, T. N. Mandal, C.-S. Lim, J. A. Chang, Y. H. Lee, H.-J. Kim, A. Sarkar, M. K. Nazeeruddin, M. Grätzel, S. I. Seok, *Nat. Photonics* **2013**, *7*, 486.
- [53] J. Burschka, N. Pellet, S.-J. Moon, *Nature* **2013**, *499*, 316.
- [54] D. Bi, S.-J. Moon, L. Häggman, G. Boschloo, L. Yang, E. M. J. Johansson, M. K. Nazeeruddin, M. Grätzel, A. Hagfeldt, *RSC Adv.* **2013**, *3*, 18762.
- [55] N. J. Jeon, J. H. Noh, Y. C. Kim, W. S. Yang, S. Ryu, S. I. Seok, *Nat. Mater.* **2014**, *13*, 897.
- [56] J.-H. Im, I.-H. Jang, N. Pellet, M. Grätzel, N.-G. Park, *Nat. Nanotechnol.* **2014**, DOI: 10.1038/NNANO.2014.181.
- [57] K.-C. Wang, J.-Y. Jeng, P.-S. Shen, Y.-C. Chang, E. W.-G. Diau, C.-H. Tsai, T.-Y. Chao, H.-C. Hsu, P.-Y. Lin, P. Chen, T.-F. Guo, T.-C. Wen, *Sci. Rep.* **2014**, *4*, 4756.
- [58] O. Malinkiewicz, A. Yella, Y. H. Lee, G. M. Espallargas, M. Graetzel, M. K. Nazeeruddin, H. J. Bolink, *Nat. Photonics* **2014**, *8*, 128.
- [59] D. Liu, T. L. Kelly, *Nat. Photonics* **2014**, *8*, 133.
- [60] Z. Zhu, Y. Bai, T. Zhang, Z. Liu, X. Long, Z. Wei, Z. Wang, L. Zhang, J. Wang, F. Yan, S. Yang, *Angew. Chem.* **2014**, *126*, 1.
- [61] P. Qin, S. Tanaka, S. Ito, N. Tetreault, K. Manabe, H. Nishino, M. K. Nazeeruddin, M. Grätzel, *Nat. Commun.* **2014**, *5*, 3834.
- [62] J. A. Christians, R. C. M. Fung, P. V. Kamat, *J. Am. Chem. Soc.* **2014**, *136*, 758.
- [63] M. M. Lee, J. Teuscher, T. Miyasaka, T. N. Murakami, H. J. Snaith, *Science* **2012**, *338*, 643.
- [64] B. Conings, L. Baeten, C. D. Dobbelaere, J. D'Haen, J. Manca, H.-G. Boyen, *Adv. Mater.* **2013**, DOI: 10.1002/adma.201304803.
- [65] M. J. Carnie, C. Charbonneau, M. L. Davies, J. Troughton, T. M. Watson, K. Wojciechowski, H. Snaith, D. A. Worsley, *Chem. Commun.* **2013**, *49*, 7893.
- [66] M. Liu, M. B. Johnston, H. J. Snaith, *Nature* **2013**, *501*, 395.
- [67] B. Cai, Y. Xing, Z. Yang, W.-H. Zhang, J. Qiu, *Energy Environ. Sci.* **2013**, *6*, 1480.
- [68] E. Edri, S. Kirmayer, D. Cahen, G. Hodes, *J. Phys. Chem. Lett.* **2013**, *4*, 897.
- [69] S. Ryu, J. H. Noh, N. J. Jeon, Y. C. Kim, W. S. Yang, J. Seo, S. I. Seok, *Energy Environ. Sci.* **2014**, *7*, 2614.
- [70] E. Edri, S. Kirmayer, M. Kulbak, G. Hodes, D. Cahen, *J. Phys. Chem. Lett.* **2014**, *5*, 429.
- [71] J. H. Noh, S. H. Im, J. H. Heo, T. N. Mandal, S. I. Seok, *Nano Lett.* **2013**, *13*, 1764.
- [72] T. M. Koh, K. Fu, Y. Fang, S. Chen, T. C. Sum, N. Mathews, S. G. Mhaisalkar, P. P. Boix, T. Baikie, *J. Phys. Chem. C* **2014**, *118*, 16458.
- [73] G. E. Eperon, S. D. Stranks, C. Menelaou, M. B. Johnston, L. M. Herz, H. J. Snaith, *Energy Environ. Sci.* **2014**, *7*, 982.
- [74] J.-W. Lee, D.-J. Seol, A.-N. Cho, N.-G. Park, *Adv. Mater.* **2014**, *26*, 4991.
- [75] N. Pellet, P. Gao, G. Gregori, T.-Y. Yang, M. K. Nazeeruddin, J. Maier, M. Grätzel, *Angew. Chem. Int. Ed.* **2014**, *53*, 3151.
- [76] N. K. Noel, S. D. Stranks, A. Abate, C. Wehrenfennig, S. Guarnera, A. A. Haghighirad, A. Sadhanala, G. E. Eperon, M. B. Johnston, A. M. Petrozza, L. M. Herz, H. J. Snaith, *Energy Environ. Sci.* **2014**, *7*, 3061.
- [77] F. Hao, C. C. Stoumpos, D. H. Cao, R. P. H. Chang, M. G. Kanatzidis, *Nat. Photonics* **2014**, *8*, 489.
- [78] Y. Ogomi, A. Morita, S. Tsukamoto, T. Saitho, N. Fujikawa, Q. Shen, T. Toyoda, K. Yoshino, S. S. Pandey, T. Ma, S. Hayase, *J. Phys. Chem. Lett.* **2014**, *5*, 1004.
- [79] J.-H. Im, H.-S. Kim, N.-G. Park, *APL Mater.* **2014**, *2*, 081510.
- [80] Y. Ma, L. Zheng, Y.-H. Chung, S. Chu, L. Xiao, Z. Chen, S. Wang, B. Qu, Q. Gong, Z. Wu, X. Hou, *Chem. Comm.* **2014**, DOI: 10.1039/c4cc01962h.
- [81] G. Juška, K. Arlauskas, M. Viliūnas, J. Kočka, *Phys. Rev. Lett.* **2000**, *84*, 4946.
- [82] M. Xiao, F. Huang, W. Huang, Y. Dkhissi, Y. Zhu, J. Etheridge, A. Gray-Weale, U. Bach, Y.-B. Cheng, L. Spiccia, *Angew. Chem.* **2014**, *126*, 10056.

- [83] Y. Wu, A. Islam, X. Yang, C. Qin, J. Liu, K. Zhang, W. Penga, L. Han, *Energy Environ. Sci.* **2014**, *7*, 2934.
- [84] C. Zuo, L. Ding, *Nanoscale* **2014**, *6*, 9935.
- [85] Q. Chen, H. Zhou, Z. Hong, S. Luo, H.-S. Duan, H.-H. Wang, Y. Liu, G. Li, Y. Yang, *J. Am. Chem. Soc.* **2014**, *136*, 622.
- [86] N. C. Greenham, R. H. Friend, D. D. C. Bradley, *Adv. Mater.* **1994**, *6*, 491.
- [87] N. C. Greenham, I. D. W. Samuel, G. R. Hayes, R. T. Phillips, Y.A.R.R. Kessener, S. C. Moratti, A. B. Holmes, R. H. Friend, *Chem. Phys. Lett.* **1995**, *241*, 89.
- [88] A. Sadhanala, F. Deschler, T. H. Thomas, S. E. Dutton, K. C. Goedel, F. C. Hanusch, M. L. Lai, U. Steiner, T. Bein, P. Docampo, D. Cahen, R. H. Friend, *J. Phys. Chem. Lett.* **2014**, *5*, 2501.
- [89] A. S. Subbiah, A. Halder, S. Ghosh, N. Mahuli, G. Hodes, S. K. Sarkar, *J. Phys. Chem. Lett.* **2014**, *5*, 1748.
- [90] V. Gonzalez-Pedro, E. J. Juarez-Perez, W.-S. Arsyad, E. M. Barea, F. Fabregat-Santiago, I. Mora-Sero, J. Bisquert, *Nano Lett.* **2014**, *14*, 888.
- [91] R. S. Sanchez, V. Gonzalez-Pedro, J.-W. Lee, N.-G. Park, Y. S. Kang, I. Mora-Sero, J. Bisquert, *J. Phys. Chem. Lett.* **2014**, *5*, 2357.
- [92] H. J. Snaith, A. Abte, J. M. Ball, G. E. Eperon, T. Leijtens, N. K. Noel, S. D. Stranks, J. T.-W. Wang, K. Wojciechowski, W. Zhang, *J. Phys. Chem. Lett.* **2014**, *5*, 1511.
- [93] H.-S. Kim, N.-G. Park, *J. Phys. Chem. Lett.* **2014**, *5*, 2927.
- [94] M. Kaltenbrunner, M. S. White, E. D. Glowacki, T. Sekitani, T. Someya, N. S. Sariciftci, S. Bauer, *Nat. Commun.* **2012**, *3*, 770.
- [95] D. J. Lipomi, Z. Bao, *Energy Environ. Sci.* **2011**, *4*, 3314.
- [96] P. Docampo, J. M. Ball, M. Darwich, G. E. Eperon, H. J. Snaith, *Nat. Commun.* **2013**, *4*, 2761.
- [97] J. You, Z. Hong, Y. Yang, Q. Chen, M. Cai, T.-B. Song, C.-C. Chen, S. Lu, Y. Liu, H. Zhou, Y. Yang, *ACS Nano* **2014**, *8*, 1674.
- [98] C. R. Carmona, O. Malinkiewicz, A. Soriano, G. M. Espallargas, A. Garcia, P. Reinecke, T. Kroyer, M. I. Dar, M. K. Nazeeruddin, H. J. Bolink, *Energy Environ. Sci.* **2014**, *7*, 994.
- [99] B. J. Kim, D. H. Kim, Y.-Y. Lee, H.-W. Shin, G. S. Han, J. S. Hong, K. Mahmood, T. K. Ahn, Y.-C. Joo, K. S. Hong, N.-G. Park, S. Lee, H. S. Jung, *Energy Environ. Sci.* **2014**, DOI: 10.1039/C4EE02441A.
- [100] S. N. Habisreutinger, T. Leijtens, G. E. Eperon, S. D. Stranks, R. J. Nicholas, H. J. Snaith, *Nano Lett.* **2014**, dx.doi.org/10.1021/nl501982b.
- [101] W.-J. Yin, T. Shi, Y. Yan, *Adv. Mater.* **2014**, *26*, 4653.

Received: September 13, 2014  
Revised: September 30, 2014  
Published online: October 30, 2014